

Article

Geochemical Characterization of and Exploration Guide for the World-Class Mafic–Siliciclastic-Hosted Touro VMS Cu Deposit, Northwestern Iberian Peninsula

Pablo Nuñez ¹, Alvaro Rubio ², Daniel Arias ², Jorge Fuertes-Blanco ², Fernando Cortés ¹, Fernando Díaz-Riopa ¹ and Agustín Martín-Izard ^{2,*}

¹ Cobre San Rafael, S.L., Santiago Avenue 42. O Pino, 15823 A Coruña, Spain; pablo.nunez@atalayamining.com (P.N.); fernando.corte@atalayamining.com (F.C.); fernando.diaz@atalayamining.com (F.D.-R.)

² Department of Geology, University of Oviedo, C/Arias de Velasco s/n, 33005 Asturias, Spain; rubioalvaro@uniovi.es (A.R.); darias@uniovi.es (D.A.); jorgefuert@gmail.com (J.F.-B.)

* Correspondence: amizard@uniovi.es

Abstract: A geochemical study was conducted on the Touro deposit, which is situated within the Iberian Variscan Massif on the allochthonous terrain of the Galicia–Tras-os-Montes Zone. This study encompassed both mineralogical and geochemical analyses of the host rocks, with a particular focus on the high-grade Fornás metamorphic unit of the Órdenes Complex. The deposit is composed of massive and semi-massive sulfides, the host rocks are amphibolites and paragneisses, and the ore is hosted in garnet amphibolites and mineralized paragneisses. A microscopic study of thin sections and over 300 electron probe microanalyses on various minerals were conducted with the objective of geochemical characterization. Furthermore, a study of approximately 6000 samples processed by mining companies for multielement analyses of over 1350 drill cores was conducted to geochemically characterize the host and mineralized rocks for use as exploration guides. Additionally, five samples underwent Sm–Nd isotope analysis. The data from the Touro Cu (Zn–Co) deposit are consistent with its classification as a mafic–siliciclastic (Besshi-type) VMS deposit constructed in a back-arc environment during the Ordovician period. Following burial and high-grade metamorphism during the Middle Devonian period, these rocks were subsequently exposed during the later Variscan deformation phases, resulting in the formation of the Arinteiro antiform.

Keywords: geochemistry; ore; host rock; VMS; Galicia–Trás-os-Montes; Variscan Iberian Massif; Touro deposit



Citation: Nuñez, P.; Rubio, A.; Arias, D.; Fuertes-Blanco, J.; Cortés, F.; Díaz-Riopa, F.; Martín-Izard, A. Geochemical Characterization of and Exploration Guide for the World-Class Mafic–Siliciclastic-Hosted Touro VMS Cu Deposit, Northwestern Iberian Peninsula. *Minerals* **2024**, *14*, 1159. <https://doi.org/10.3390/min14111159>

Academic Editors: Stavros Triantafyllidis and Stylianos Tombros

Received: 20 September 2024
Revised: 13 November 2024
Accepted: 14 November 2024
Published: 16 November 2024



Copyright: © 2024 by the authors. Licensee MDPI, Basel, Switzerland. This article is an open access article distributed under the terms and conditions of the Creative Commons Attribution (CC BY) license (<https://creativecommons.org/licenses/by/4.0/>).

1. Introduction

A number of recent studies have been conducted on Touro ore, including investigations of the ore body itself [1–7], as well as studies on the region in which it is located from a geological perspective [8–14]. One of these studies [1] also includes a comprehensive geological description of the area, the deposit, and its location within the NW of the Iberian Massif, as well as an account of the history of mineral exploration and mining in the region. The work [1] encompasses the geometry and 3D modeling of the ore body, the petrography of the mineralized and host rocks, and the potential geodynamic location of the deposit, as well as information on ore prospecting and environmental management. Nevertheless, no prior studies have addressed the mineralogical and geochemical characterization of the host rocks, ore, and surrounding hydrothermally altered rocks. In order to gain an accurate understanding of the geological characteristics of the area in question, it is necessary to consider a number of factors, including the fact that the deposit and host rocks have undergone intense metamorphism in the amphibolite facies and were significantly deformed by the Variscan orogeny.

To characterize the mineralogy, a supplementary study was conducted on 24 thin sections using an optical microscope, employing both transmitted and reflected light on polished thin sections. This study was conducted as a follow-up to those previously conducted by the authors of [1], in which a number of minerals were subjected to a multielemental analysis of over 300 electron probe microanalyses (EPMAs) in order to geochemically characterize them.

The results allowed for the mineralogical characterization of the entire range of rocks that were involved in the formation of the deposit, which allowed us to confirm the suitability of the previously proposed geodynamic model [1,4,7] of a VMS deposit of the mafic–siliciclastic type [15] (Besshi-type) and to determine the mineralogical differences between the host rocks and hydrothermally mineralized rocks, the latter of which can be used as a prospecting guide for geological areas with similar geological characteristics.

In order to achieve this objective, approximately 6000 samples from more than 1350 drill cores were employed, which underwent multielemental analyses by the mining companies. The mining companies extracted samples from the drill cores in a systematic manner, with the objective of identifying and distinguishing the four main lithologies present: amphibolite, paragneiss, mineralized amphibolite, and mineralized paragneiss. The geochemical data provided by the companies include those on the elements of the greatest economic interest (e.g., Cu, Zn, Pb, As) and other elements included in the analytical routines. As the aforementioned analyses did not include some of the elements commonly used to determine the rock source and igneous origin, nor those needed to validate the previous analyses, we conducted 25 analyses of the major and trace elements, REEs, and Sm–Nd isotopes on five of the samples. Furthermore, a comparison was conducted between the current results and data from previously published regional studies from the area [9,16–18].

Given the markedly metamorphosed and deformed nature of the rocks under examination [4,8], which can exhibit gradual transitions and geochemical modifications during the sedimentation, exhalation, and hydrothermal processes, an additional objective was to identify the elements that could assist in distinguishing between the various lithologies and hydrothermal alterations. In this regard, the elements Th, Ca, Sr, and Ba, and the accompanying diagrams using several elements, proved particularly useful.

Geotectonic Setting

The geological setting of the deposit is delineated in [1–4], which present summaries of the most salient data pertaining to the area. The Variscan orogeny, which occurred during the collision between Gondwana and Laurussia, led to the development of the Iberian Massif during the Devonian–Permian period (400–290 million years ago) (Figure 1A) [19–21]. In Galicia, the European Variscan suture is well represented and includes allochthonous remnants of fragments with both continental and oceanic affinities, which demonstrate structural interrelationships between them [22,23]. The Iberian Massif is distinguished by its arcuate configuration, or the “Asturian arc”, which is the result of the emergence of a secondary oroclinal type during the latter stages of the Variscan orogeny (the Moscovian to Asselian, approximately 310–297 Ma), which affected all the previous structures. The oroclinal geometry, which developed during the Laurussia–Gondwana collision, gave way to the formation of the Pangea supercontinent at the end of the Carboniferous–Early Permian period [24,25], a closure that was accompanied by the formation of other structures. The zone is composed of a variety of geological features, including fragments of a passive continental margin, zones that have undergone rifting processes, rocks of a volcanic arc and back-arc basins, and ophiolite units [20–23,26–34]. As a result, the northwestern region of the Iberian Peninsula was shaped by the convergence and amalgamation of diverse geological terrains, including one that was autochthonous to the area and several that were not. The latter are evident in the core of the Late Variscan synclines that constitute the Galicia–Trás-os-Montes Zone [13]. Three allochthonous complexes have been identified: the Cabo Ortegal Complex, the Órdenes Complex, and, in the west, the Malpica–Tuy unit

(Figure 1B). Furthermore, two additional complexes are situated within the Portuguese Trás-os-Montes region: the Bragança and Morais complexes. The Órdenes Complex is the largest of the Galician allochthonous complexes, with an approximate area of 135 km by 75 km, and its rounded geometry is a consequence of its synform shape. A range of tectono-metamorphic processes have affected the Galicia–Trás-os-Montes Zone, as evidenced by the available geological data [1].

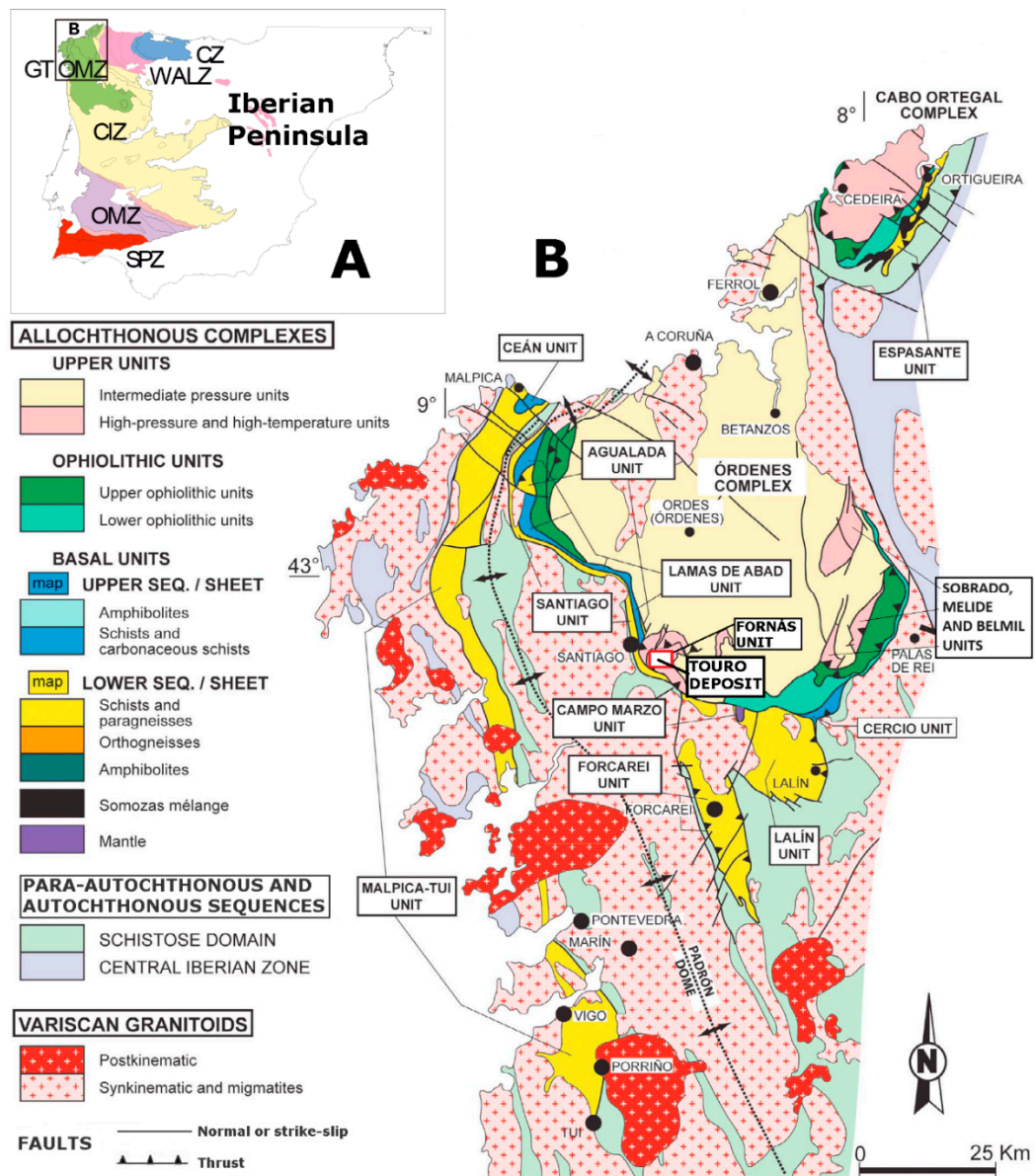


Figure 1. (A) Geological map of the Iberian Variscan Massif. CZ: Cantabrian Zone; WALZ: West Asturian–Leonese Zone; CIZ: Central Iberian Zone; OMZ: Ossa Morena Zone; SPZ: South Portuguese Zone. (B) The following geological map of the NW Iberian Massif illustrates the positions of the various allochthonous units of the Galicia–Trás-os-Montes Zone and Central Iberian Zone. Additionally, the location of the Touro deposit is indicated. From [1], adapted from [9].

The aforementioned fragments exhibit characteristics that are indicative of their original position, lithological composition, and tectonothermal evolution, and they can be grouped into three members: the basal, ophiolitic, and upper members. Both the basal and upper members display a continental crustal lithological composition, including an island arc and back-arc basins. The upper member comprises two submembers: the high-pressure–high-temperature (HP-HT) unit at the base and the medium-pressure (MP) unit

at the top. The Touro deposit is located within the HP-HT submember. In contrast, the ophiolitic units are derived from an oceanic crust (see Figure 1B). In a few instances, minor mineralized bodies are associated with these units, as observed in the Moeche area within the Cabo Ortegal member [35]. All of these units are separated from one another by tectonic detachments from the top downwards through the Corredoiras, Fornás, and Bembibre–Ceán formations.

The geodynamic context for the formation of the magmatic (tholeiitic/alkaline) rocks of the HP-HT units is a volcanic magmatic arc and back-arc extensional basin [8,23–27]. Several deformation processes during this process have been recorded. The most commonly observed lithologies in the HP-HT member are paragneisses and metamafic–ultramafic rocks, including garnet and clinopyroxene granulites and eclogites, as well as their retrograde metamorphic equivalents, such as amphibolites and greenschists [16–18]. The Fornás unit, in which the Touro deposit is situated, is distinguished by the prevalence of amphibolites hosted within the paragneisses. These amphibolites contain relict textures of gabbro rock, as indicated in [8], but the most common are amphibolites with relicts of granulite minerals (Cpx-Grt-Pl, [6]) and metagabbros and metaperidotites, which exhibit a range of retrogradation, from almost untransformed to coronitic metagabbros and granulites [36] and pyroxenites. The chemical composition of the gabbros is tholeiitic, exhibiting characteristics comparable to those of Mid-Ocean Ridge Basalt (MORB) [37]. The intermediate-pressure unit and the HP-HT unit are separated by the Corredoiras detachment [21,38].

The Touro deposit and other mineralized areas in the vicinity occur in the HP-HT lower member of the upper units. It is postulated that the primary metamorphic event (HP-HT) is associated with a preliminary subduction episode that occurred contemporaneously with the advent of the Variscan deformation (D1). This unit has been described in five distinct localities: Sobrado, Melide, and Belmil, situated in the southeastern region of the Órdenes Complex, and Arinteiro and Fornás, which are located in the south. The latter has been identified as the host of the Touro deposit. The mean copper content is 0.41%, as estimated by the company (Atalaya Mining), with a total resource of 103 Mt [1,37]. The evaluation method, its associated uncertainties, and the resulting data are accessible via the Internet [39]. Some authors [4,7] have considered the possibility that the geological context for the Touro deposit could be a metamorphosed Besshi-type ore (siliciclastic–mafic [15]) but have ultimately proposed a Cyprus-type (mafic [15]) metamorphosed ophiolitic VMS deposit for Touro.

2. Materials and Methods

The whole-rock analyses (mineralized and unmineralized) were performed by ALS Limited (Vancouver, Canada, Accredited Laboratory No. 579) on materials provided to them by the mining companies between 2013 and 2017, using the Ultra-Trace Level Method ME-MS61, which entails a four-acid digestion process coupled with the utilization of ICP-MS instrumentation. Subsequently, the final solution is subjected to analysis by means of inductively coupled plasma atomic emission spectrometry and inductively coupled plasma mass spectrometry. The results are corrected for spectral interferences. Previously, the authors of [1] employed some of these analyses, namely, 270 data points for Fe, Ti, Al, and Mn from the Arca deposit. The elements analyzed by the mining companies in percentages were Al, Ca, Cu, Fe, K, Mg, Na, Ti, S, and Zn, and the elements analyzed in ppm were Au, Ag, As, Ba, Be, Bi, Cd, Ce, Co, Cr, Cs, Cu, Ga, Ge, Hf, In, La, Li, Mn, Mo, Nb, Ni, P, Pb, Rb, Re, Sb, Sc, Se, Sn, Sr, Ta, Te, Th, Tl, U, V, W, Y, Zn, and Zr. For a comprehensive account of the findings, please refer to the Supplemental Data Files, which are lettered A to D.

Twenty-four polished, thin sections were prepared and examined by means of transmitted and/or reflected light microscopy, scanning electron microscopy with energy-dispersive X-ray spectroscopy (JEOL-6610LV, Tokyo, Japan), and electron probe microanalysis (EPMA) (Cameca SX100) at the University of Oviedo (Spain). The major elements were determined at accelerating potentials of 15 and 20 kV, beam currents of 15 and 20 nA, and an acquisition

time between 10 and 20 s for both the X-ray peak and background. The standard deviation of the results for all the electron microprobe analyses was found to be less than 0.1%.

The elements analyzed for mineral characterization via EPMA were K, Ca, Ti, Fe, Mn, Na, Si, Mg, Al, P, Cl, F, Cr, and Ni. Quantitative analyses were calibrated using certified natural and synthetic standards. The acquired X-ray intensities were corrected for atomic number, mass absorption, and secondary fluorescence effects using the CAMECA x-phi program, which allows for the correction of X-ray intensities for a variety of effects. The results are presented in Supplementary E.

To corroborate the findings of the preceding analyses, supplementary analyses (Supplementary F) were conducted on 25 non-mineralized samples collected from a considerable distance from the mineralized regions, which exhibited no visible mineralization. The objective of these analyses was to confirm the geochemical attributes of the non-mineralized rocks. The analyses permitted the geochemical characterization of both mafic and paragneiss rocks, and they were conducted using X-ray fluorescence, with lithium metaborate (LiBO_2) employed as the melter for the samples at the SCT of the University of Oviedo. Whole-rock trace element analyses were conducted using inductively coupled plasma mass spectrometry (ICP-MS) at the Geochronology and Isotope Geochemistry SGIker facility of the UPV/EHU, employing methodologies adapted from those described in detail in [40]. The reagents employed were concentrated HF and HNO_3 (Merck Pro-Analysi, Darmstadt, Germany). Deionized water was obtained using a Millipore Elix device and polished to achieve a resistivity of at least 18 MOhm-cm using the Barnstead Easy Pure system. The internal standard solutions of In and Bi and the multielemental solutions employed for the initial tuning and calibration of the spectrometer were prepared from PerkinElmer multielement standard solutions for ICP stabilized in HNO_3 at a concentration of 2 to 6%. An automatic online addition kit was employed to introduce the internal standard, thereby preventing the introduction of random errors. The dilutions were performed with the utmost precision, down to 0.1 mg, using an electronic balance (GRAM SV 205-A). The alkaline fusion of the samples was conducted using an automated Claisse Fluxy 30 system, employing butane gas in Pt-Au (95-5) crucibles with lithium metaborate (LiBO_2) as the fluxing agent and LiBr as the non-wetting agent. The molten material was automatically poured into a polystyrene beaker containing 100 mL of nitric acid and approximately 0.05 mL of hydrofluoric acid, which was placed in a magnetic agitator. The solution was then gravimetrically diluted to an appropriate factor for the intended analysis.

The trace element concentrations were determined using a Thermo XSeries 2 ICP-MS (Waltham, MA, USA), which was equipped with a collision cell (an interphase specific for elevated total dissolved solids, or Xt cones), a shielded torch, and a gas dilution system. A concentric PFA nebulizer and quartz expansion chamber were utilized. Further details on the instrumental method can be found in [40]. The outcomes for the CRMs and the projected margins of error for each component are presented in the table of results in the Supplementary Material (Supplementary F). These were calculated using the error propagation equation in [41].

The Sm-Nd isotope geology analyses were conducted using isotope dilution thermal ionization mass spectrometry (ID-TIMS) and were performed at the SGIker facility of the University of the Basque Country/EHU (Spain) using a fully automated Finnigan MAT262 mass spectrometer. The chemical procedures for the Sm and Nd extraction are described in [42]. A $^{150}\text{Nd}/^{149}\text{Sm}$ mixed-isotope tracer was used. Blanks for Sm and Nd were negligible, and the two elements were loaded over Ta filaments. The measurements were taken using Faraday stages in a multicollection system, with corrections for mass fractionation via normalization to $^{146}\text{Nd}/^{144}\text{Nd} = 0.7219$. The analytical uncertainty was estimated to be $\pm 0.2\%$ on the $^{147}\text{Sm}/^{144}\text{Nd}$ ratio, and the uncertainty for individual measurements was estimated under the same conditions as those of the $^{143}\text{Nd}/^{144}\text{Nd}$ and $^{143}\text{Nd}/^{144}\text{Nd}$ ratios for the La Jolla standard over different analysis periods.

3. Ore Deposit Geology (Previous Studies)

The geology of the ore deposit (Figure 2) was previously investigated by [1], who conducted preliminary mineralogical and petrographic research. Our study made use of the data collected by the authors [1], which served as the foundation for the research presented here. The aforementioned authors identified two principal groups of rocks, and for the purposes of the geochemical study, the samples were grouped according to these two categories: mafic igneous rocks, which encompass a number of amphibolite types, pyroxenite (metagabbro), and paragneisses. Both groups of samples exhibit hydrothermal alteration during the mineralization process, resulting in the formation of garnet amphibolites and mineralized paragneisses in proximity to or containing the ores after metamorphism.

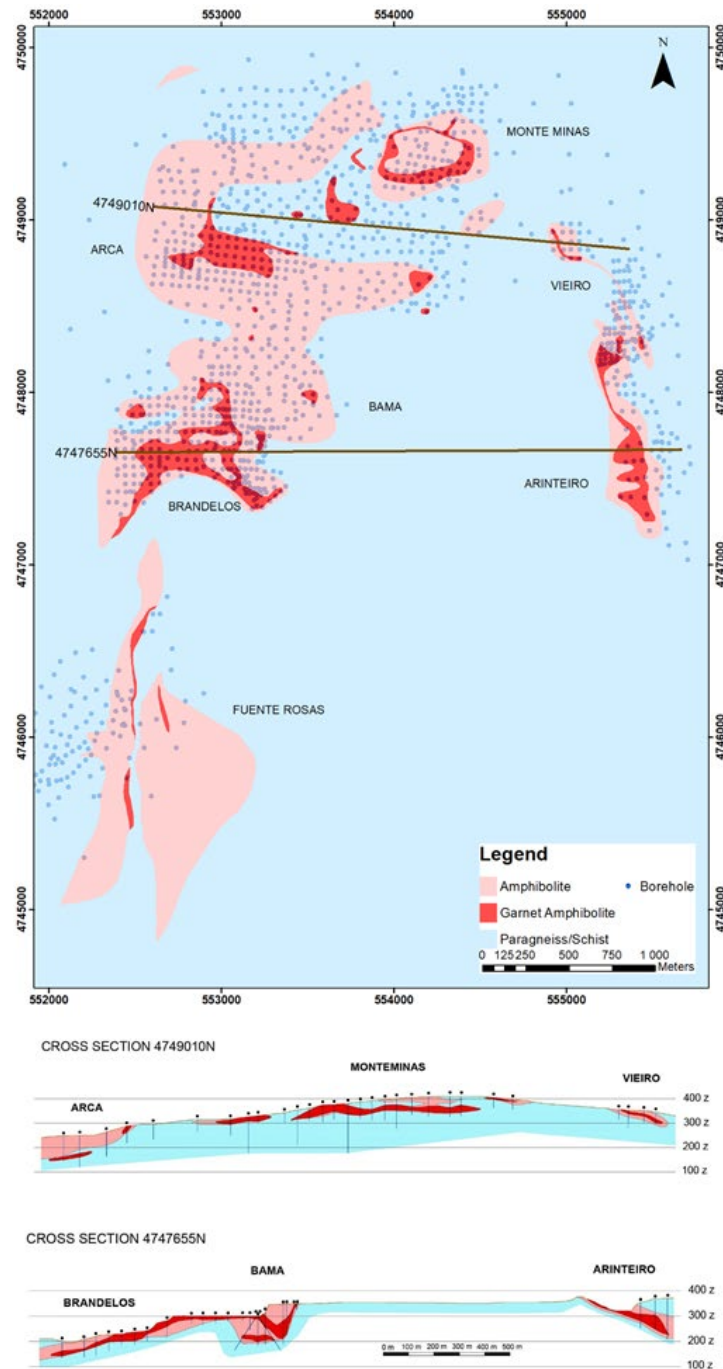


Figure 2. Geological map and cross sections of the Touro copper deposit, from [3].

As previously stated in [1], a microscopic investigation enabled the identification of two distinct amphibolite varieties: a fine-grained, dark-green amphibolite and a garnet-rich, porphyritic amphibolite. The first is a banded amphibolite comprising hornblende and plagioclase, with minor amounts of chlorite, epidote, pyroxene, and rare garnet. The texture is ophitic, defined by the presence of hornblende crystals. The amphibolite is in contact with the paragneisses at both the upper and lower levels of the bodies. In the majority of instances, the garnet-rich, porphyritic amphibolite is situated in close proximity to the fine-grained, dark-green amphibolite. The texture is porphyritic to nematoblastic; it is notable for its Ca-poor composition, and it is directly related to the mineralized ore bodies. The rock is composed of chlorite, quartz, and almandine garnet up to 3 cm in diameter, with minor amounts of hornblende, plagioclase, actinolite, rutile, and epidote–zoisite, and abundant opaque minerals, mostly pyrrhotite, chalcopyrite, and minor sphalerite and pyrite. Approximately 25%–35% of the rock is composed of garnet, and there is transition amphibolite between the aforementioned amphibolite types.

As defined in [1], the paragneisses exhibit a fine to medium grain size, a dark coloration, a lepidoblastic texture, and a mineral composition comprising quartz, biotite, plagioclase, garnets, and graphite with minor muscovite, staurolite, sillimanite, kyanite, rutile, and ilmenite and scarce sulfides (pyrrhotite and pyrite). The paragneisses display a banded structure, comprising alternating plagioclase layers and quartz-rich levels with mica-rich levels, which, in turn, contain graphite and sulfides.

The mineralized structures [1] at the outcrop (massive sulfides and stringers) are predominantly tabular in shape, reaching a maximum thickness of 100 m, and they are subhorizontal, exhibiting distinct contact with the host rock. The mineralized structures extend approximately 6 km along the limbs and hinge zone of the Arinteiro N–S-trending antiform (Figure 2). The Touro deposit has been subdivided by Atalaya Mining and the authors of [1] into seven principal economic ore bodies, which have been designated Arinteiro, Vieiro, Arca, Monte Mina, Bama, Brandelos, and Fuente Rosas. It should be noted that several of these bodies are contiguous at depth.

In all the ore bodies, the mineralized mass is primarily hosted by garnet amphibolites. However, mineralized bodies are also present in the paragneisses situated below the amphibolites in the Arca and Monte das Minas areas. The mineralization can be classified as either massive sulfides, with a minimal presence of non-sulfide minerals dispersed throughout the rock, or semi-massive sulfides. In the latter case, it can have a brecciated texture, consisting of brecciated zones in both garnet amphibolites and mineralized paragneisses. These zones were initially identified in [1] as stringer zones, and they contain fragments of rock comprising plagioclase, phlogopite, hornblende, clinozoisite, epidote, and quartz, which are cemented by pyrrhotite–chalcopyrite. In reference to the aforementioned rock fragments, the authors of [4,7] proposed the designation “rolled balls”. The richest zones of zinc (up to 0.47%) are associated with this mineralization, and no lead minerals were identified.

4. Results

4.1. Petrography

The following section presents the petrography and microprobe results. During the core description, two groups of amphibolites and paragneisses were identified: normal and garnet-rich amphibolites and paragneisses and mineralized paragneisses, a distinction that is evident from a mineralogical and petrographic perspective.

4.1.1. Amphibolite

The amphibolite lithology, represented by four samples, is characterized by a green color and fine-grained, granoblastic texture. The major minerals identified include hornblende, zoisite–clinozoisite, epidote s.s., quartz, plagioclase, and, in one thin section, grossularite garnet. Furthermore, trace minerals were identified, including pyrrhotite, pyrite, ilmenite, and titanite, as well as local staurolite. The secondary minerals include chlorite

and carbonates. In specific localities, the rock exhibits partial nematoblastic hornblende-rich and clinozoisite–quartz bands. The garnet observed in this lithology, situated in an area in close proximity (several centimeters) to the mineralized garnet amphibolites, differs from that observed in the paragneisses and garnet amphibolites, as it is an accessory mineral and exhibits a relatively small size (less than 100 microns).

4.1.2. Garnet Amphibolite

Of particular interest is the garnet amphibolite, which is the principal mineralized rock. A total of eight samples were examined, exhibiting a range of textures, including granoblastic and grano-lepidoblastic, and in some instances, brecciated and cemented by sulfides (stringers). The garnets were found within a dark-green, fine-grained matrix. Upon microscopic examination, the rock was observed to be grano-lepidoblastic, comprising large garnet crystals within a matrix predominantly composed of chlorite, with lesser quantities of epidote–zoisite, tremolite, actinolite, hornblende, and quartz. The associated minerals are potassium feldspar and rutile, and the opaque minerals are pyrrhotite, sphalerite, chalcopyrite, ilmenite, and pyrite. Garnet is often poikiloblastic and fractured, yet unaltered. The micaceous minerals of the matrix display partial orientation, predominantly around the garnets. As indicated in [1,43], the microstructural analyses suggest that the foliation in all the rocks gives rise to S-type mylonites, which may be indicative of inhomogeneous pure shearing or flattening. The primary opaque mineral is pyrrhotite, which contains chalcopyrite, minor pyrite, and transparent minerals. The chalcopyrite crystals are irregular in shape and range in size from 10 to 100 microns. In this lithological formation, there are some late-stage interstitial and carbonate veins that traverse the other minerals and are up to 0.5 mm thick.

4.1.3. Paragneiss

Paragneiss is a lithological formation that is distinguished by a granoblastic structure, which comprises alternating bands of opaque minerals and micaceous bands. A total of eight samples were examined. The principal minerals are garnet, quartz, feldspar, biotite–phlogopite, and muscovite. Furthermore, the following accessory minerals are present: titanite, apatite, staurolite, chlorite (an alteration product of biotite), and opaque minerals, primarily graphite, sphalerite, pyrrhotite, and, on occasion, chalcopyrite, which is included in the latter. Pyrite is also present in the sample, derived from the replacement of pyrrhotite. Garnet is often fractured but not altered, and the mica minerals present in the matrix are oriented to a limited extent, predominantly around the garnets. As is the case with garnet amphibolites, foliation in all rocks produces S-type mylonites, which suggests inhomogeneous pure shearing or flattening. The graphite- and sulfide-rich bands are derived from organic-rich sediments (black shales), whereas the mica-rich levels originate from a shale with a low organic content.

4.1.4. Mineralized Paragneiss

In a considerable number of instances, this lithological composition, from which four samples were examined, exhibits a brecciated texture, comprising fragments of paragneiss within a sulfide matrix and cement, which is predominantly pyrrhotite (stringers). The fragments are composed of K-feldspar (microcline), phlogopite (with some biotite), minor actinolite, and quartz. The principal sulfides are pyrrhotite, chalcopyrite, ilmenite, arsenopyrite, and pyrite, the latter of which is derived from the replacement of pyrrhotite. The larger fragments were designated “rolled balls” in [4], while the smaller fragments are predominantly quartz, with occasional occurrences of zoisite.

4.2. Microprobe Results

In order to characterize the various minerals, over 300 analyses were conducted on eight polished sections, comprising three amphibolites, three garnet amphibolites, two paragneisses, and one mineralized paragneiss. The structural formula was calculated based

on the obtained analyses, and the results were projected onto the mineral classification diagrams (Figure 3A–F) from [44–47].

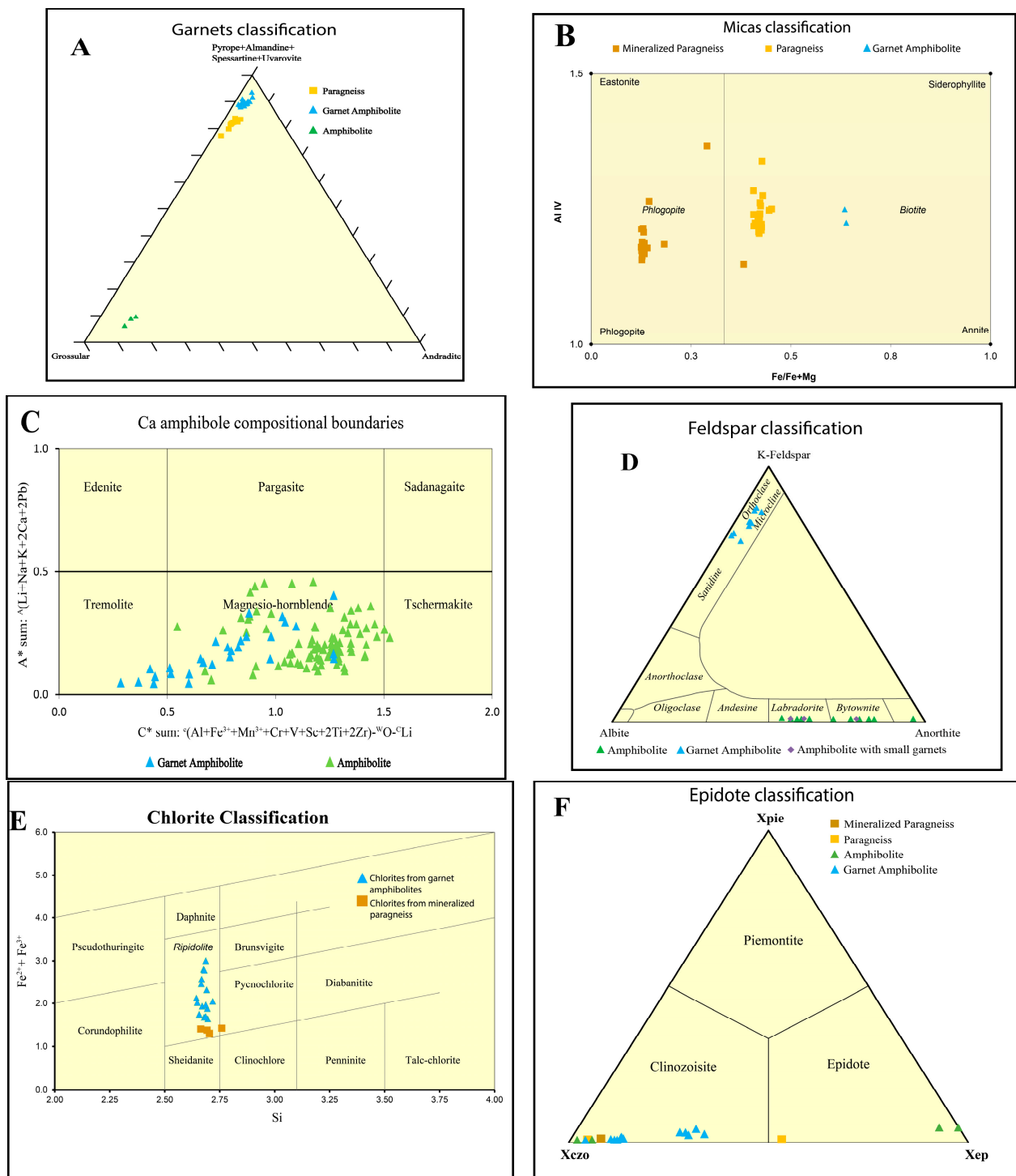


Figure 3. Microprobe results: (A) garnet classification; (B) mica classification; (C) amphibole classification; (D) feldspar classification; (E) chlorite classification; (F) epidote classification [44–47].

4.2.1. Garnets

The chemical results of the garnets from the various lithologies are distributed across different fields, yet, within each lithology, they are situated in a consistent area (Figure 3A). The larger garnet crystals from garnet-rich amphibolites and paragneisses plot in a distinct

field, yet they are all pyrope–almandine, exhibiting the lowest calcium content among the garnet amphibolites and a relatively higher calcium concentration in the paragneisses. The small garnet crystals present in the fine-grain amphibolites are wholly distinct, exhibiting a grossularite composition.

4.2.2. Micas

Three distinct types of mica (Figure 3B) were identified in the geological samples: phlogopite in mineralized paragneiss breccias, magnesium-rich biotite in paragneiss, and iron-rich biotite in garnet-rich amphibolite. Micas also facilitate clear differentiation between the three rock types that contain this mineral. The mineralized paragneiss contains a magnesium-rich mica, while the garnet amphibolite contains magnesium-poor mica.

4.2.3. Amphibole

The majority of the analyzed amphiboles are Mg–hornblende, exhibiting an evolutionary progression from the tschermakite boundary to tremolite (Figure 3C, adapted from the amphibole classification diagram in [44]). Indeed, microscopic observation revealed a replacement of hornblende by tremolite from amphibolite to mineralized amphibolite (garnet amphibolite), which is consistent with the loss of calcium in the mineralized garnet amphibolites.

4.2.4. Feldspars

In the present study, we analyzed feldspar from two distinct lithological sources: amphibolite and garnet amphibolite. The feldspars in these two lithologies display notable dissimilarities, as illustrated in Figure 3D. The plagioclases from the amphibolites are distinguished by a high calcium content and are primarily composed of labradorite–bytownite. The plagioclase is identical in the amphibolite, with the presence of minor grossularite garnets, which indicates that the rock is the same. In contrast, the feldspars in the garnet amphibolites are characterized by a high alkali content and plot in the microcline–orthoclase field.

4.2.5. Chlorite

The chlorites under examination were derived from mineralized rocks, specifically garnet amphibolites and mineralized paragneisses. As could be observed under a microscope, the majority of the analyzed chlorites were frequently associated with epidote, which is also a secondary mineral that develops during retrometamorphism.

The results indicate that the majority of the analyzed chlorites are ripidolite, with the exception of a single sample of picnochlorite, which falls just on the border with ripidolite (Figure 3E). The geothermometer used in [48] was applied to the chlorites, yielding temperatures of approximately 365 °C during the retrometamorphism process.

4.2.6. Epidote

All of the studied rocks contain epidote, though the varieties present in each rock type differ (Figure 3F). The minerals subjected to analysis were clinozoisite and epidote. The latter was observed exclusively in the paragneiss, where it co-occurred with clinozoisite. The majority of the analyzed epidotes are clinozoisite, with a considerable proportion originating from garnet amphibolite, where two distinct varieties are identified. The sole epidote identified within the paragneiss sample is situated at the borderline between the epidote and clinozoisite fields.

4.2.7. Carbonates

According to the microprobe analyses, the carbonates present in the veins cutting the mineralized rocks (garnet amphibolites and mineralized paragneisses, including the breccias) or filling open spaces can be categorized into two distinct types: an iron-rich siderite type, which is the most abundant, and a calcium-rich calcite type (Table 1). The

presence of carbonates has the potential to modify the geochemistry of the rocks, and this possibility was incorporated into the analytical framework.

Table 1. Microprobe analyses of carbonates (MP: mineralized paragneiss; GA: garnet amphibolite). Given the limited number of carbonate types, a table is a more appropriate representation than a graph.

	GA Siderite	MP Siderite	GA Siderite	MP Siderite	GA Siderite	MP Calcite	GA Calcite	GA Calcite								
MgO	0.46	0.43	0.45	0.49	0.56	0.6	0.6	0.51	0.51	0.42	0.56	0.17	0.6	0.39	0.27	
CaO	6.23	5.3	5.91	5.78	5.49	5.78	5.79	5.63	5.63	5.92	3.2	4.94	59.78	60.98	60.43	
MnO	1.17	1.19	1.26	1.15	1.02	1.28	1.12	1.18	1.18	1.15	0.33	0.93	0.36	0.44	1.16	
FeO	52.44	53.48	52.97	53.13	53.59	52.99	53.41	53.66	53.66	53.81	57.17	55.79	0.73	0.47	0.39	
Total	60.43	60.56	60.67	60.71	60.77	61.08	61.09	61.18	61.18	61.34	61.46	62.08	62.45	63.13	64.04	

4.3. Whole-Rock Geochemical Analyses

A comprehensive geochemical and whole-rock analysis, coupled with a detailed hydrothermal alteration study, was conducted. The samples can be classified into two main categories: non-mineralized (amphibolites and paragneisses) and mineralized (garnet amphibolites and mineralized paragneisses). From the comprehensive set of analytical results and potential graphical representations, we selected the most notable graphs and diagrams, which are described in detail within the text.

To ensure the reliability of the samples used exclusively for rock classification purposes, those that underwent significant hydrothermal mineralization and transformation were excluded, including garnet amphibolites and mineralized paragneisses. Notwithstanding, these samples were integrated into the remaining graphs to demonstrate the influence of hydrothermal alteration. The mining company provided the following rock analyses: 1855 from metabasalts and metagabbros (1778 amphibolites and 77 pyroxenites), 2337 from garnet amphibolites, 1773 from paragneisses, and 412 from mineralized paragneisses. To ensure a comprehensive evaluation of the data, an additional 25 analyses (Supplementary E) were conducted and integrated with the results provided by the mining company.

After an exhaustive examination of the available data (see Supplementary G, bivariate X-Y plots), it was determined that the most effective method for differentiating between the various rock types in the mineralized areas was the graph that employs the Th vs. Ba + Sr ratio (Figure 4), utilizing the complete data set (comprising over 6000 samples). The aforementioned diagram allowed for a clear distinction between the paragneisses, mineralized paragneisses (hydrothermally altered paragneisses), and metabasic rocks based on their Th contents.

Furthermore, the diagram allows for the differentiation between metamorphosed metabasic rocks and metamorphosed hydrothermally altered metabasic rocks (garnet-rich amphibolite) based on their Ba + Sr contents. The rock classification was conducted during the visual core logging, which may have resulted in the misclassification of some rare samples and their appearances in incorrect fields. Other plots, such as the Ca vs. Ba + Sr plot, do permit the distinction between these rock types, albeit with less clarity (Figure 5).

The data projections derived from the 25 samples analyzed in this study are in alignment with the rest of the data set and thereby provide validation (Figures 4 and 5). In addition to copper and zinc, the economic element analysis revealed the presence of cobalt, which exhibited a relatively high concentration and approximately the same distribution as that of Cu. As has been demonstrated, thorium is an effective element for differentiating the various types of rocks (Figure 4). Therefore, we projected thorium vs. copper and cobalt. As illustrated in Figure 6, the Cu vs. Th diagram reveals a close relationship between the Cu content and garnet amphibolites and mineralized paragneisses.

The Th vs. Co diagram (Figure 7) exhibits a striking resemblance to those employing Cu, suggesting a correlation between copper and cobalt mineralization. Consequently, a Cu vs. Co diagram was constructed (Figure 8), which illustrates the intimate relationship between Cu and Co mineralization.

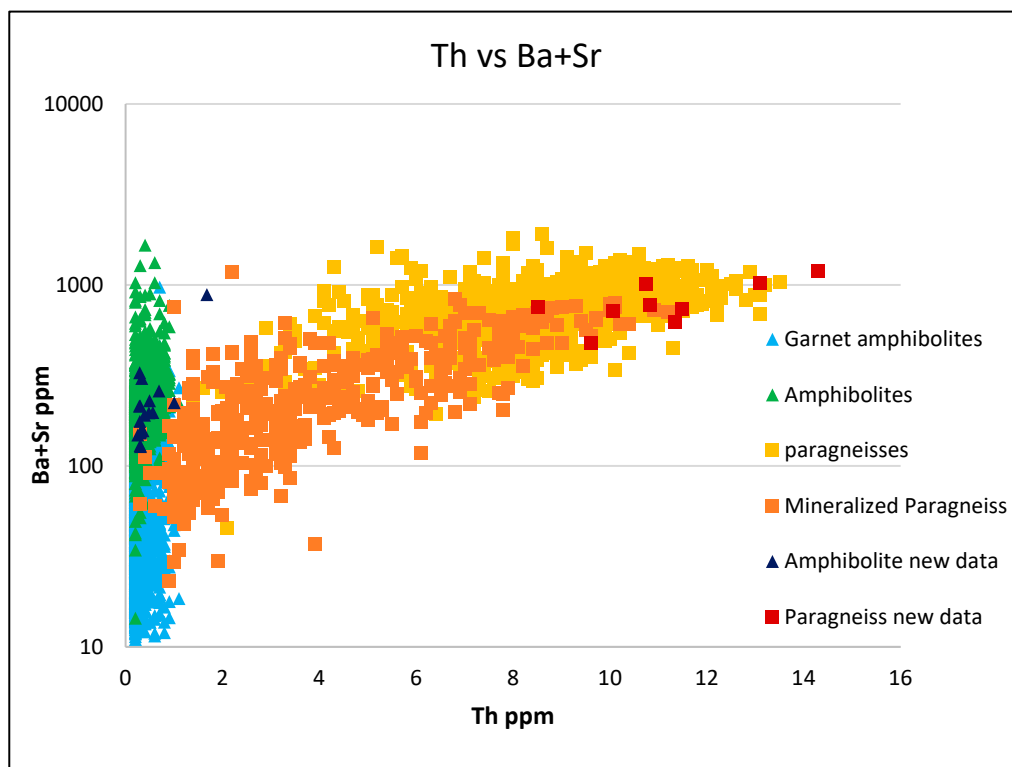


Figure 4. Th vs. Ba + Sr binary diagram allowing for the differentiation of each type of rock plot in a distinct area. Furthermore, the plot of the 25 additional samples analyzed by our team is consistent with the expected results.

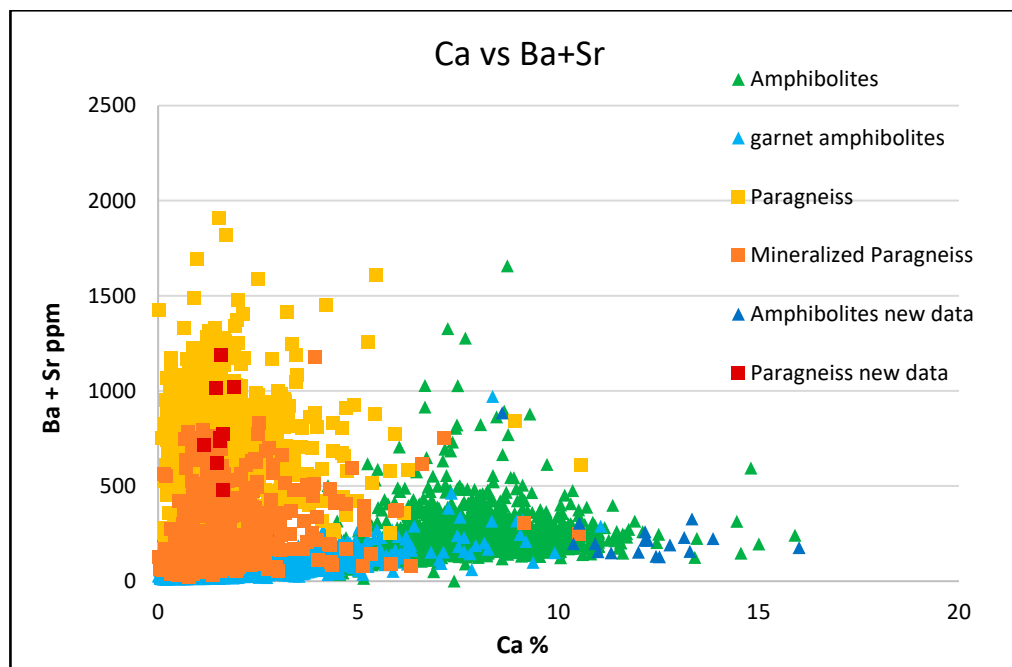


Figure 5. Ca vs. Ba + Sr binary diagram permitting the distinction between the rock types, albeit with less clarity than that afforded by Figure 4.

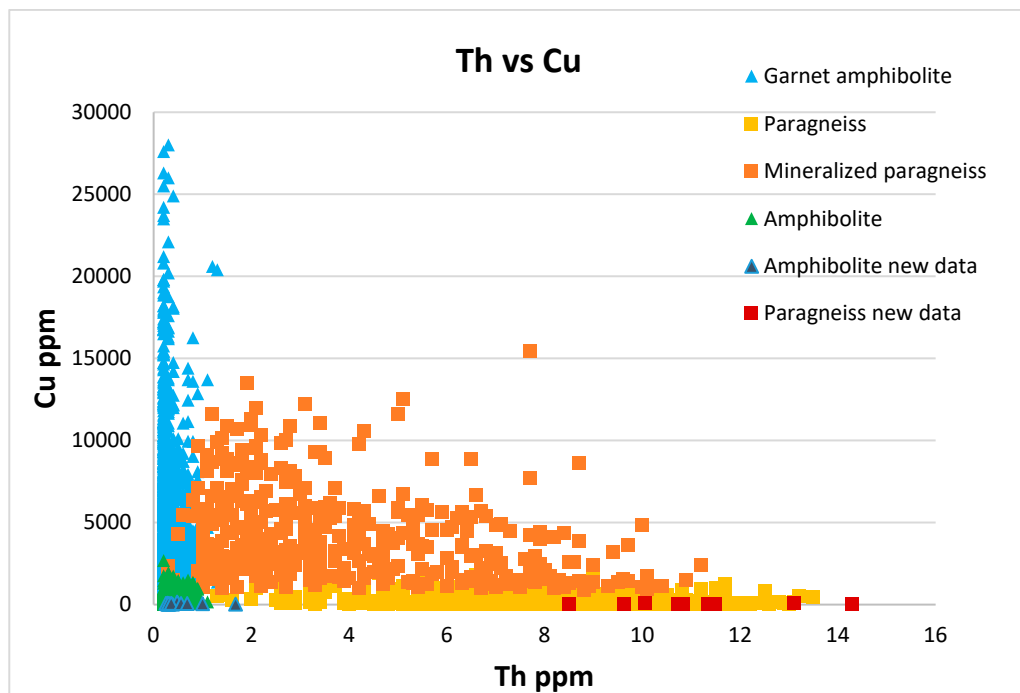


Figure 6. Cu vs. Th binary diagram demonstrating a strong correlation between the Cu content and the occurrences of garnet amphibolites and mineralized paragneisses. The recently obtained 24 samples were incorporated into the relevant lithological groups.

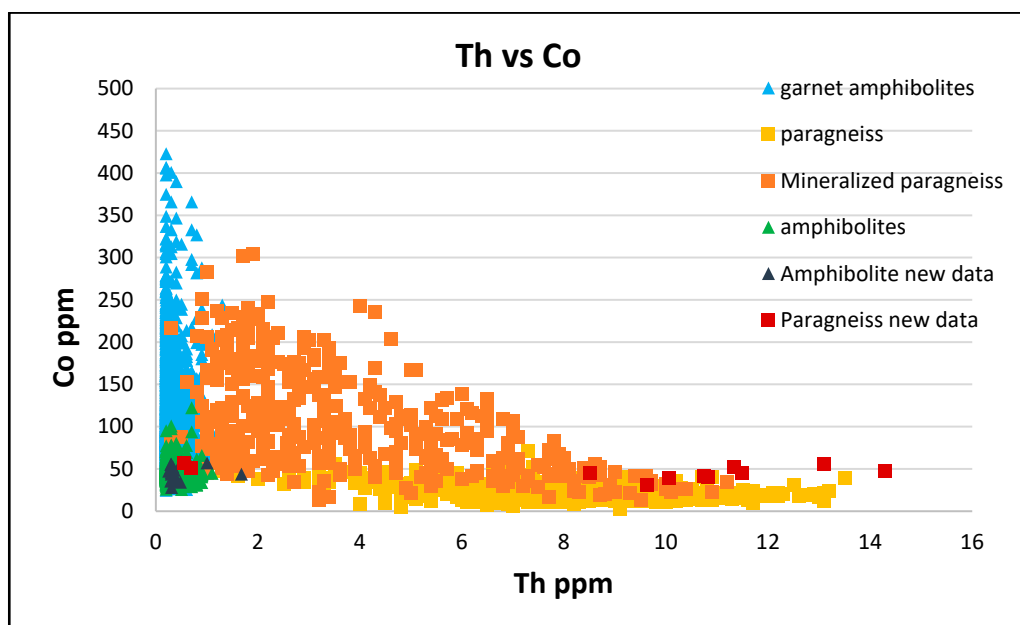


Figure 7. Th vs. Co binary diagram of the studied samples exhibits a striking resemblance to those employing Cu, suggesting a correlation between copper and cobalt. The recently obtained 24 samples were incorporated into the relevant lithological groups.

In accordance with the methodology proposed by the authors of [1], who present a limited plot of the Arca deposit, we plotted all the geochemical results in an Al/(Al + Fe + Mn) vs. Fe/Ti plot (Figure 9), as originally proposed in [49] and subsequently modified in [50,51]. As illustrated in the figure, the majority of paragneisses are situated within a cluster over pelagic and terrigenous sediments of the Pacific Ocean. Furthermore, the majority of amphibolites are situated at the mean MORB value. In contrast, both mineralized

garnet amphibolites and paragneisses display a distinct propensity for intermixing with metalliferous sediments that bear a resemblance to those observed in the Red Sea and East Pacific Rise.

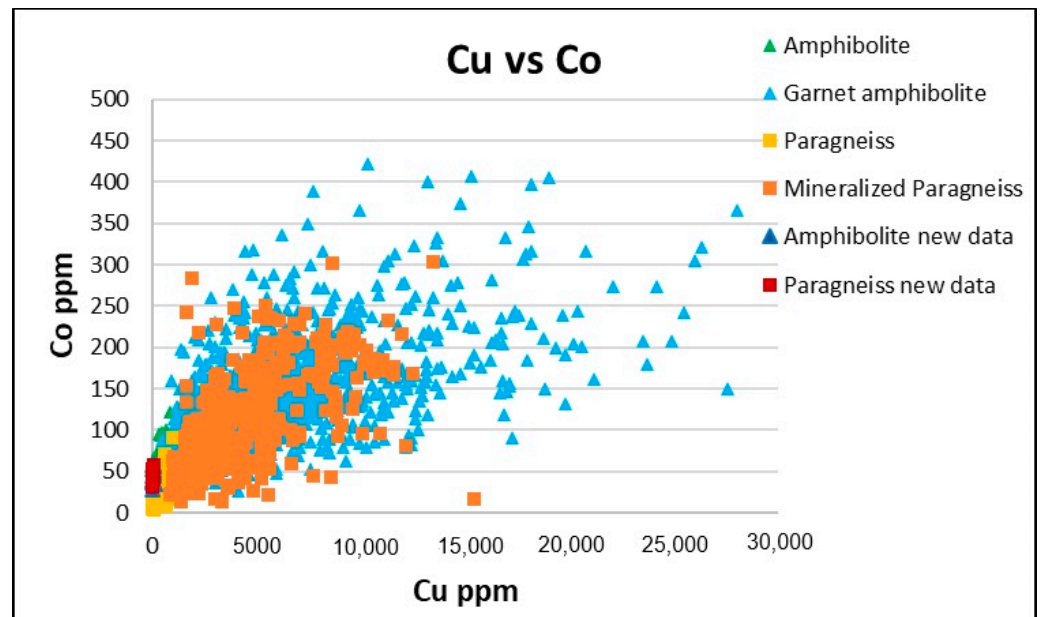


Figure 8. Cu vs. Co binary diagram of the studied samples, which illustrates the intimate relationship between Cu and Co mineralization.

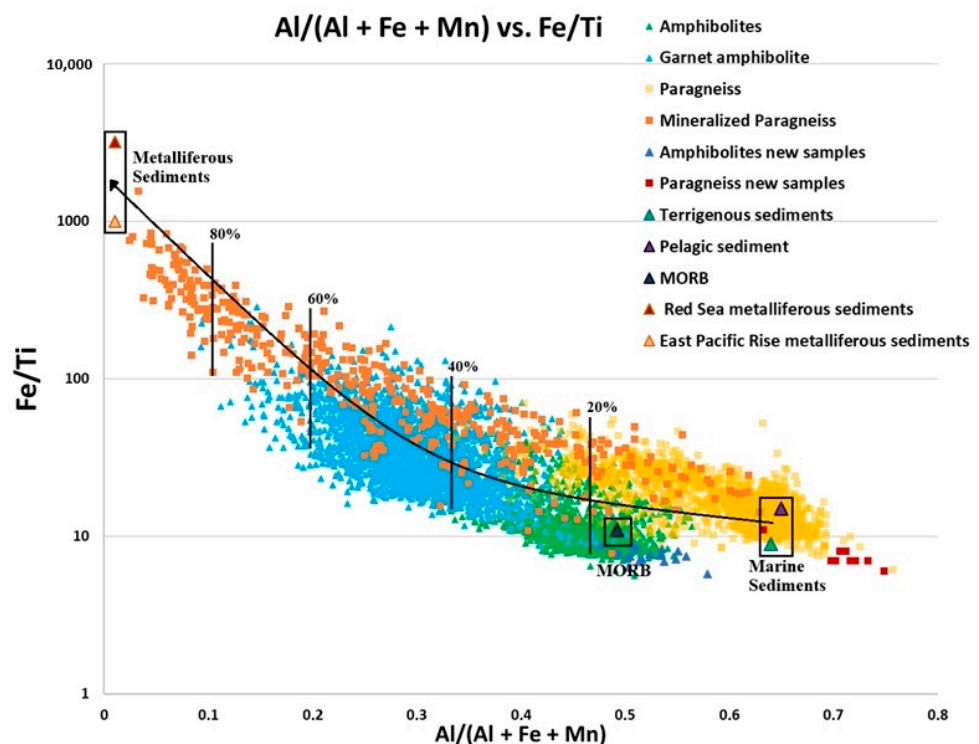


Figure 9. Al/(Al + Fe + Mn) vs. Fe/Ti plot from the Touro deposit [49] subsequently modified in [50,51]. The average compositions for metalliferous sediments from the Red Sea and East Pacific Rise, pelagic sediment from the Pacific Ocean, and terrigenous sediments [50] and the average MORB value are also shown for reference. The vertical lines indicate the percentage of mixing between the marine and metalliferous sediments.

The representation of the samples in an FeO + MgO vs. TiO₂ diagram (Figure 10) allows for the clear recognition of the trend defined by the hydrothermal alteration due to the mineralization process, which is markedly evident in the paragneisses. Furthermore, the diagram enables the observation of the extensive chemical superposition between the samples identified as paragneisses and those identified as amphibolites, a topic that will be addressed subsequently.

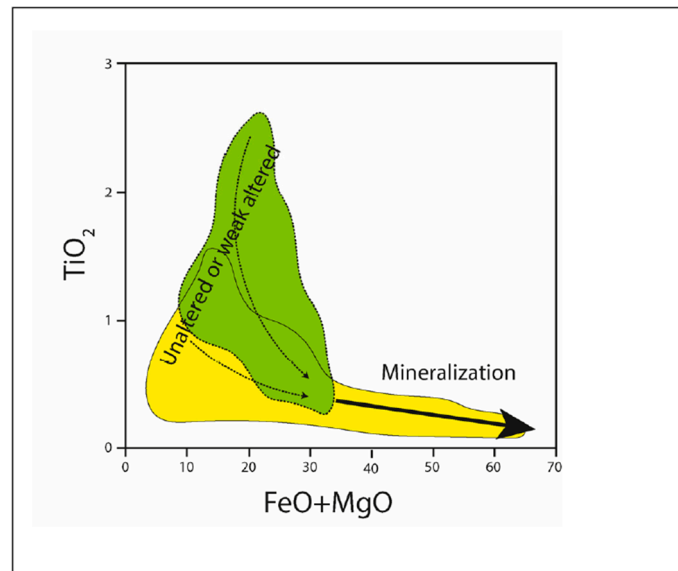


Figure 10. A FeO + MgO vs. TiO₂ plot illustrating the chemical modification of rocks (yellow: paragneisses; green: amphibolites) resulting from the introduction of Fe into the system during the mineralization process.

4.3.1. Geochemistry and Petrogenetic Characterization of Metabasic Rocks

To characterize the metabasic rocks, we employed a variety of diagrams and data from non-hydrothermally altered rocks to attain a comprehensive understanding of the subject matter.

With regard to the binary diagrams, the variations in the selected groups of elements in relation to MgO were plotted for all the unmineralized mafic igneous rocks (Figure 11). Additionally, the diagrams illustrate the outcomes for the garnet amphibolites; however, this is not within the scope of the present discussion and will be addressed in the subsequent points. The chemical composition of the amphibolites exhibits considerable variation in terms of the major elements, with magnesium and calcium concentrations ranging from 1 to 20% and from 3 to 22%, respectively. The metagabbro variability is more limited, with magnesium and calcium varying between 7 and 16% and between 0.5 and 9%, respectively. Both the amphibolites and metagabbros exhibit compositional continuity, as evidenced by the negative correlation between MgO and CaO. The metagabbros exhibit the highest magnesium oxide (MgO) contents. Similarly, there is a negative correlation between Al₂O₃, Na₂O, and MnO and CaO, resulting in greater dispersion in the rocks with the highest MgO contents.

The selected trace elements display a range of disparate patterns. A negative correlation is observed between strontium (Sr) and yttrium (Y), accompanied by a considerable degree of dispersion in the rocks with low magnesium oxide (MgO) contents. The behavior of Cr, Ni, and Ba is bimodal, exhibiting no variation with the MgO content in some instances and a positive correlation in others. The thorium concentration does not demonstrate a correlation with the magnesium oxide content. As will be discussed subsequently, the thorium content allows for the differentiation of mafic igneous rocks from paragneisses and hydrothermally altered paragneisses.

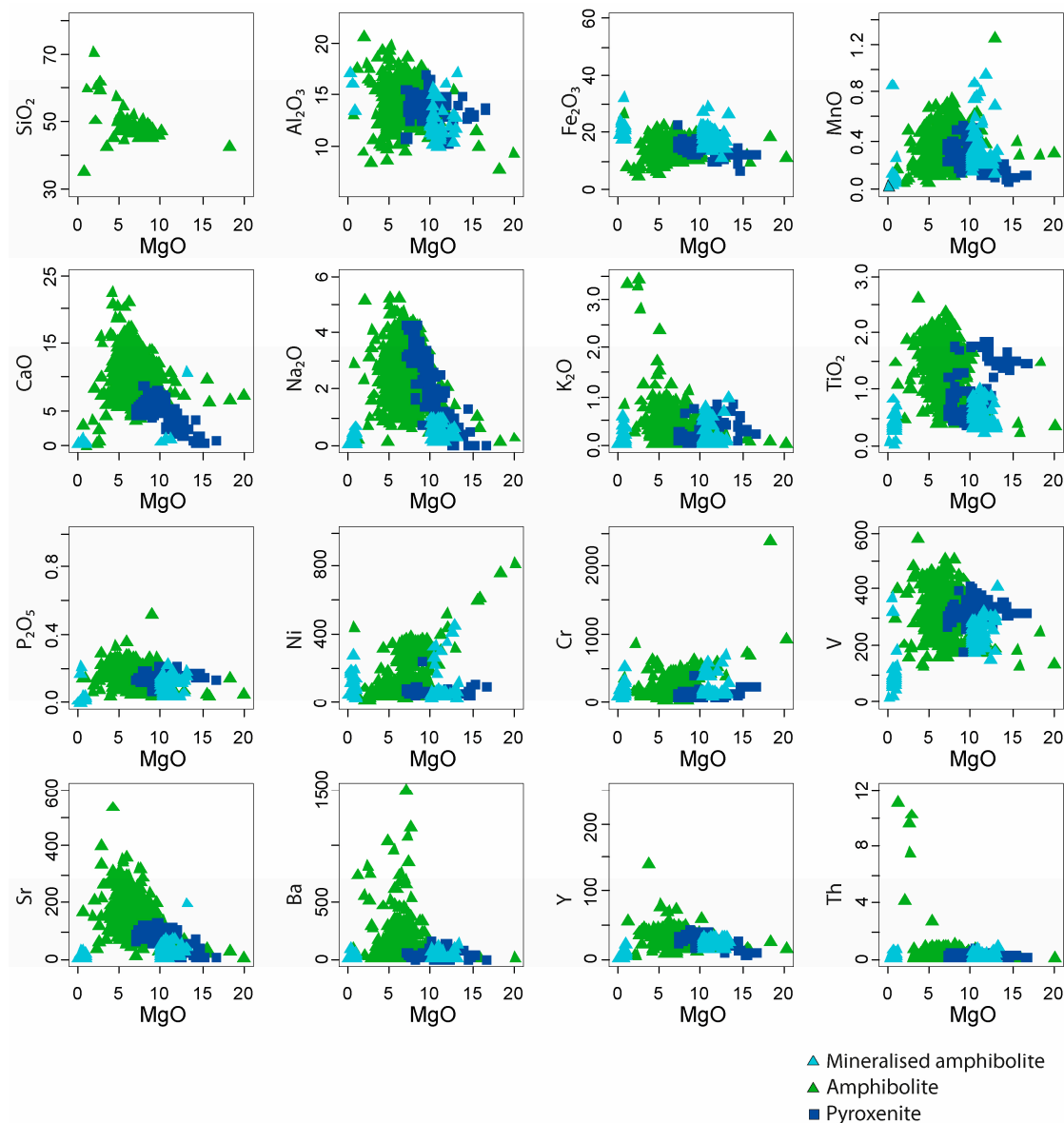


Figure 11. Diagrams showing the variation in selected groups of elements vs. MgO for unmineralized mafic igneous rocks: metabasalts (amphibolites) in blue, metagabbros (pyroxenites) in green. It should be noted that the available SiO₂ analyses are limited to a subset of samples.

Other diagrams that are useful for determining the igneous rock setting (Figure 12A) are the alkali sums of the mafic rocks, which exhibit very low values, indicating that these rocks are of a subalkaline nature. The mafic rocks analyzed correspond to a tholeiitic series, as indicated by the AFM diagram [52] (Figure 12B), with the majority of samples plotting in close proximity to the FeO-MgO side of the diagram.

As illustrated in the Th-Co diagram [53] (Figure 13), the samples are situated at the boundary between the calc-alkaline and tholeiitic fields. The authors of [16] previously proposed that this phenomenon can be attributed to the disparate positioning of the rocks in relation to the subduction zone. However, their analysis encompasses a more diverse array of rock types than those identified in the present study. As will be demonstrated subsequently, the Th content enables the differentiation of mafic igneous rocks from hydrothermally altered paragneisses.

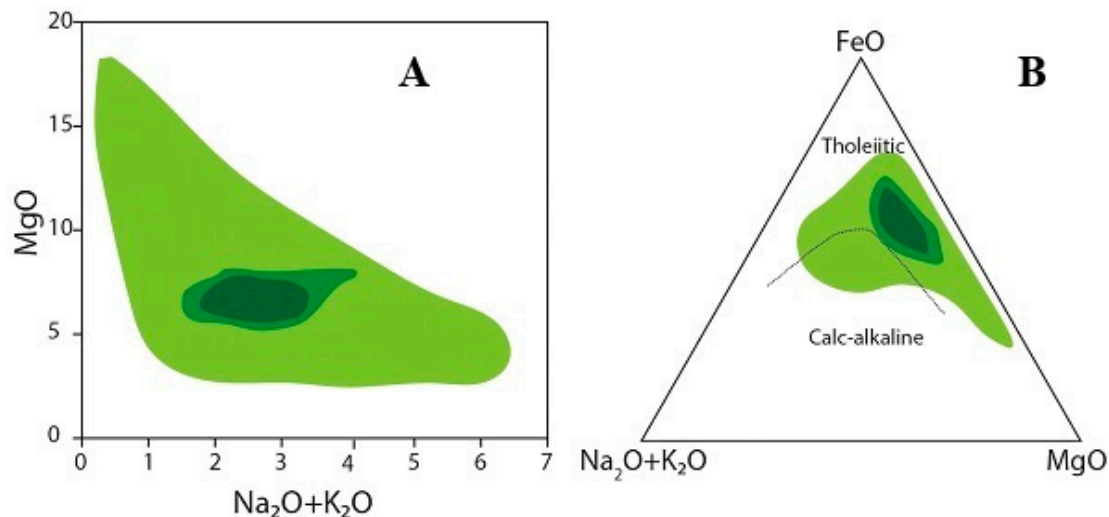


Figure 12. (A) Na + K vs. Mg binary diagram, which compares metabasic rock values of Na₂O and K₂O with those of MgO, demonstrates that the majority of the data points fall below the 4% threshold for alkali values. (B) FeO-MgO-Na₂O + K₂O ternary diagram of [52] depicts an AFM plot with the same samples, which was utilized for the subalkaline igneous rock characterization, indicating their tholeiitic nature. The green limits indicate the percentage of data, with the darker-green color indicating the highest percentage range.

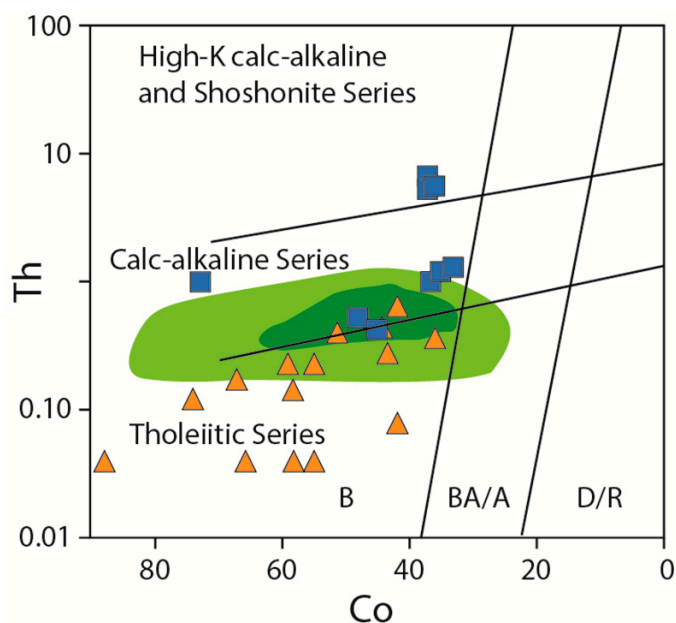


Figure 13. Th-Co binary diagram [53]. The green limits indicate the percentage of data falling within the following ranges: 0%–5%, 5%–10%, and over 10%. The squares and triangles represent mafic rocks from the Corredoiras and Monte Castelo units, respectively (data sourced from [16]). The samples are situated at the boundary between the calc-alkaline and tholeiitic fields (B: basalts; BA/A: basalt andesite/andesite; D/R: dacite/rhyolite).

In order to ascertain the alteration grade of the mafic rocks, as will be discussed subsequently, the $100 \times K_2O/Na_2O + K_2O$ vs. $Na_2O + K_2O$ plot (Figure 14) was used, which demonstrates that a number of samples have undergone a limited degree of alteration. However, the majority of the mafic samples fall within the range of unaltered samples, thereby confirming the efficacy of the sampling process.

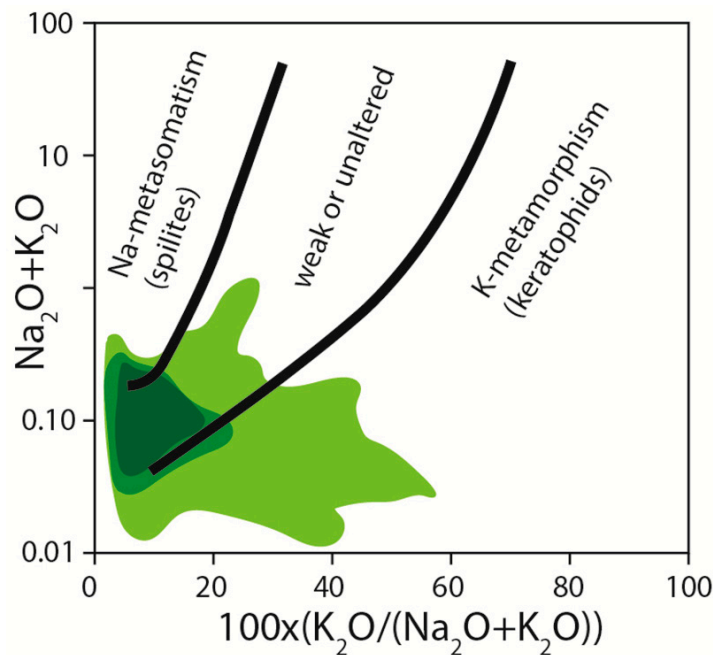


Figure 14. A $100 \times K_2O/Na_2O + K_2O$ vs. $Na_2O + K_2O$ plot was constructed to examine the hydrothermal alteration potential of the mafic rocks. The green limits indicate the percentage of data within the following ranges: 0%–5%, 5%–10%, and over 10%. The majority of the mafic samples fall within the range of unaltered samples.

To determine the tectonic setting of the samples, the Hf/3-Th-Nb/16 diagram [54] (Figure 15) was also used. The diagram illustrates a notable degree of data dispersion, with the majority of samples positioned within the E-MORB and intraplate tholeiitic fields, which is consistent with the proposed back-arc tectonic setting [9,18].

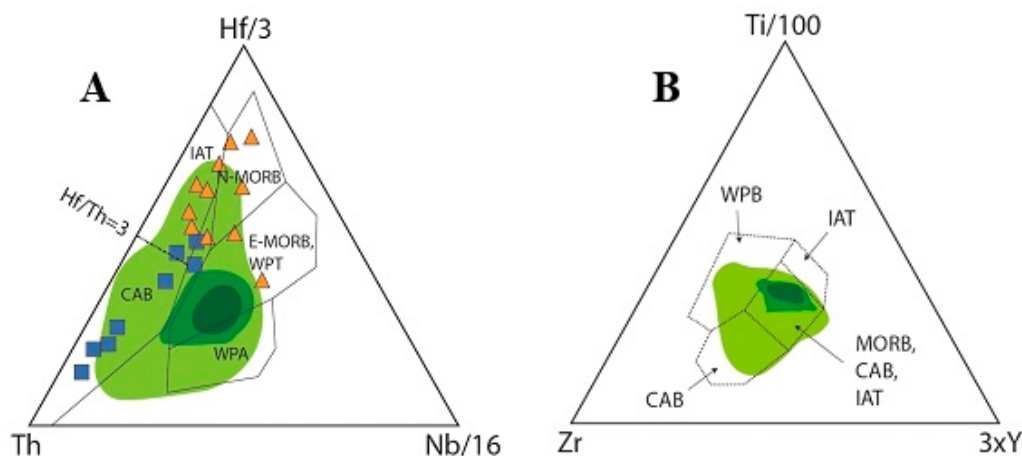


Figure 15. (A) Hf/3-Th-Nb/16 ternary diagram [54]. (B) Ti/100-Zr-3*Y ternary diagram [55]. The green limits indicate the percentage of data within the following ranges: 0%–5%, 5%–10%, and over 10%. Squares and triangles are as in Figure 13 (data from [16,23]). The diagrams (A,B) illustrate the degree of data dispersion, with the majority of samples positioned within the E-MORB and intraplate tholeiitic fields consistent with the back-arc tectonic setting.

A comparison of our results with those of [16,23] indicates that our study is limited by the fact that we analyzed only one group of samples: those taken from the area surrounding the ore body. Furthermore, the primary plot of our samples differs from that of [16,23], providing evidence that the magmatism in the area is more heterogeneous, consistent with the characteristics of a back-arc tectonic environment [16,23]. A multielement diagram

normalized to the N-MORB standard [56] (Figure 16) illustrates a consistent behavior without any deviation with regard to some of the most incompatible elements. Notably, there is a substantial depletion of Rb and Sr, and particularly of Nb. Conversely, there is evidence of enrichment in the thorium and lead concentrations. These observations may indicate a subduction tectonic event with a magmatic arc or, more likely in this case, a back arc [16,17,19].

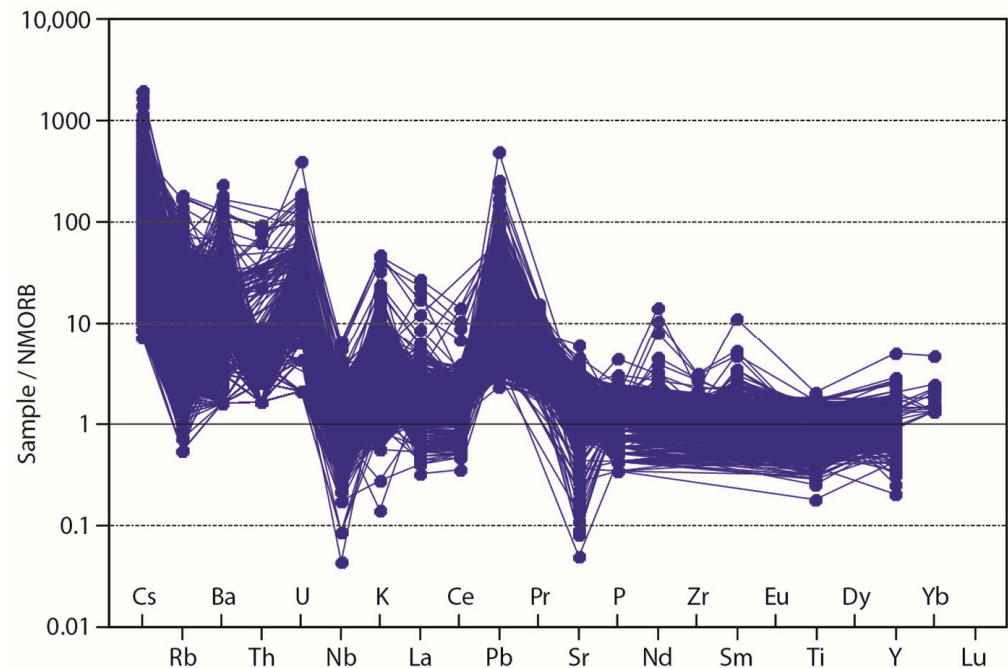


Figure 16. Spider diagram for amphibolites normalized to the N-MORB standard [56].

4.3.2. Geochemistry and Petrogenetic Characterization of Mineralized Garnet Amphibolites

As previously stated, two primary groups of amphibolites were identified: a metamorphosed MORB-type basalt and a mineralized garnet-rich amphibolite, which was determined to be a metamorphosed hydrothermally transformed basalt. This transformation involved the removal of specific elements during the hydrothermal process, namely, calcium (Ca) and barium plus strontium (Ba + Sr). Therefore, the garnet amphibolites exhibit a notable absence of calcium (and Ba and Sr), accompanied by a discernible increase in other elements, including iron, alongside other elements of particular economic interest, such as copper and cobalt.

With regard to the binary diagrams, the variation in the selected groups of elements in relation to MgO was plotted for the mafic igneous rocks (Figure 17), including the mineralized garnet amphibolites. The mineralization process results in the loss of Al, Ti, and V, as well as, to a lesser extent, alkalis. The differentiation of other elements is less discernible, and, conversely, they demonstrate notable increases in their contents, as evidenced by the Fe, Mn, and Ni. The remaining elements remain unaltered throughout the mineralization process.

4.3.3. Geochemistry and Petrogenetic Characterization of Paragneisses and Mineralized Paragneisses

In the description of the cores, two main groups of paragneisses were identified: conventional and mineralized paragneisses, a distinction that was corroborated via geochemical analysis, whereby certain elements proved particularly informative, notably Th. The conventional paragneisses typically exhibit thorium (Th) contents exceeding 6 parts per million (ppm), whereas the majority of the mineralized paragneisses display Th contents below 6 ppm. As with amphibolites, some samples fall in an intermediate position or

exhibit only a few of the main values due to the visual classification or their intermediate position (e.g., poorly mineralized). The differentiation of other elements is less discernible. Accordingly, binary diagrams (Figure 18) were constructed using thorium in conjunction with other elements for further analysis.

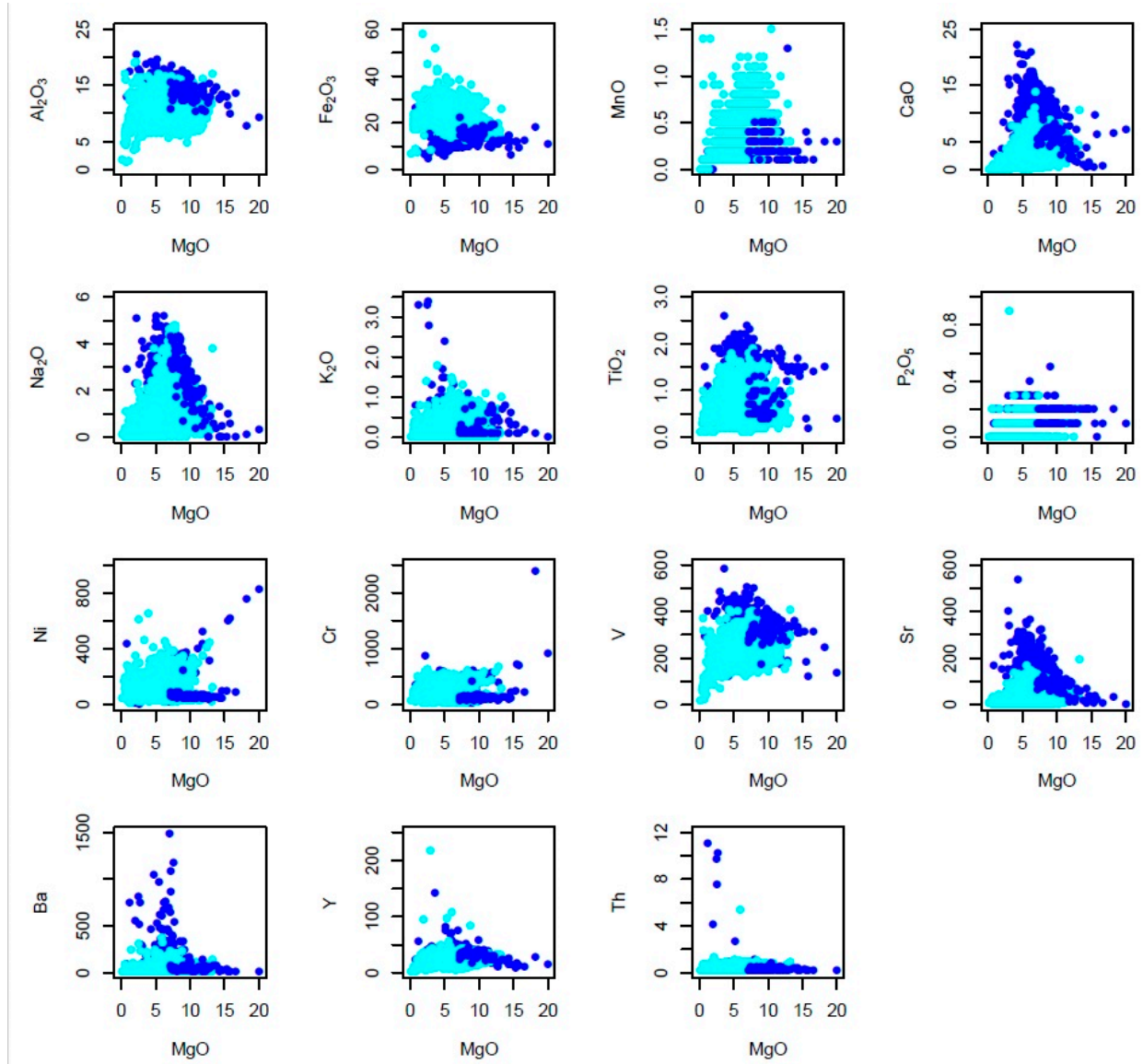


Figure 17. Binary diagrams illustrating the variation in the selected groups of elements vs. MgO for amphibolites (in dark blue) and mineralized garnet amphibolites (in pale blue), which may exhibit varying degrees of mineralization.

The binary diagrams illustrate the manner in which specific elements are mobilized or diluted during the mineralization process, while others demonstrate increases in their contents. Certain major elements, including Al_2O_3 , Na_2O , and K_2O , exhibit notable declines in their concentrations. Similarly, some trace elements, including barium (Ba) and strontium (Sr), also exhibit notable reductions in their levels. Conversely, other elements exhibit marked increases in their contents, as observed in the cases of Fe_2O_3 , Cu, Ni, and Co. The remaining elements remain unaltered throughout the mineralization process.

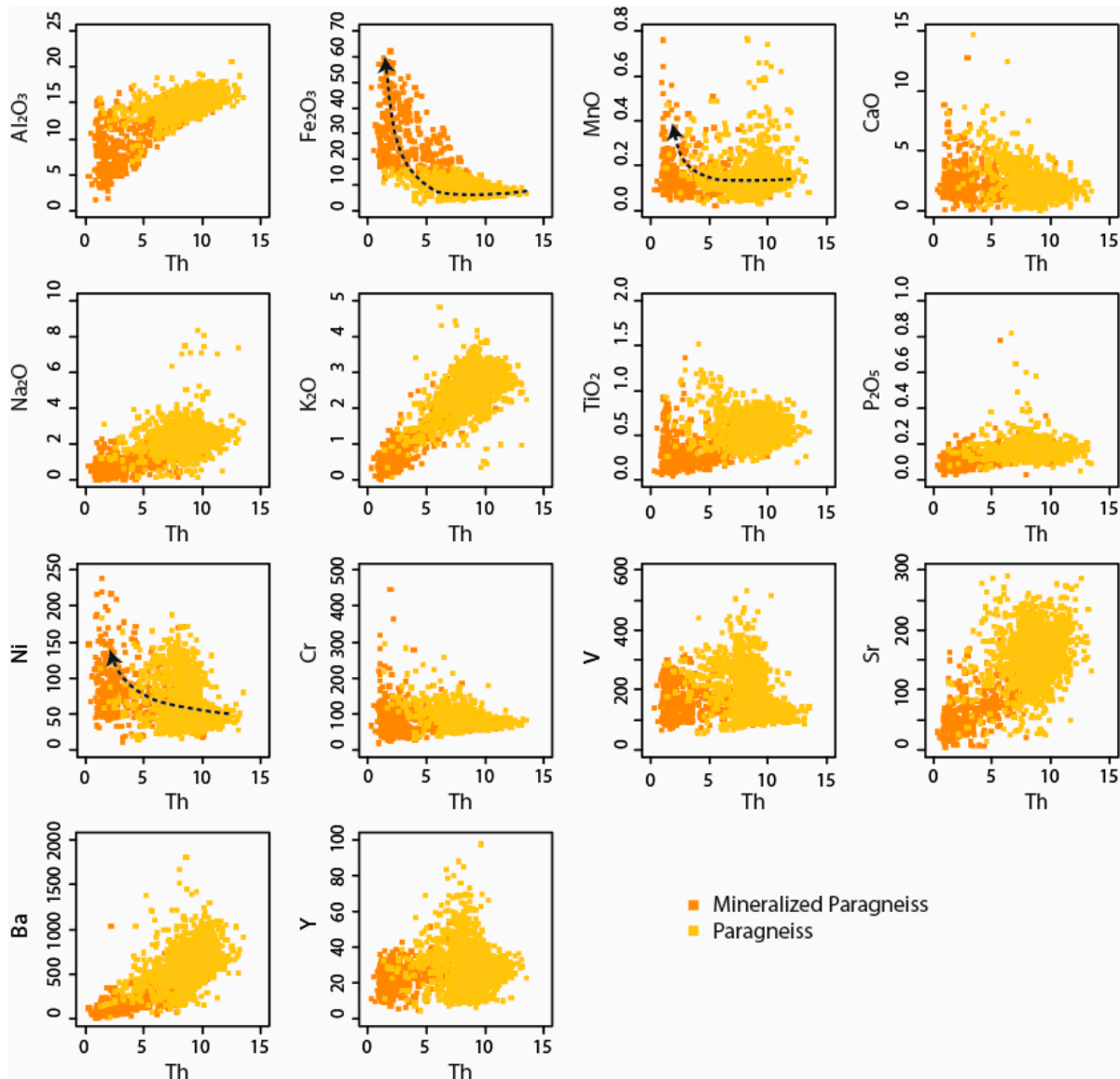


Figure 18. Binary diagrams illustrating the variation in the selected groups of elements vs. Th for unmineralized (in yellow) and mineralized (in orange) paragneisses, which may exhibit varying degrees of mineralization.

The MORB-normalized diagram of incompatible elements [56] (Figure 19) for these metasedimentary rocks illustrates a pronounced fractionation from lithophile elements to heavy rare earth elements (REEs). This trend is consistent across both non-mineralized and mineralized paragneisses, where the mineralized rocks exhibit a reduction in their element contents due to the incorporation of additional elements during mineralization. The graph illustrates notable elevations in the thorium (Th) and lead (Pb) concentrations, accompanied by negative anomalies in the neodymium (Nb) and strontium (Sr) levels, suggesting a discernible correlation with materials originating from a volcanic arc [16–18,54,55].

The paragneiss diagram is comparable to those of the mafic rocks, exhibiting the highest degree of fractionation but displaying identical anomalies, thereby indicating a common origin, a consistency that suggests that the material source is a volcanic arc [54,55].

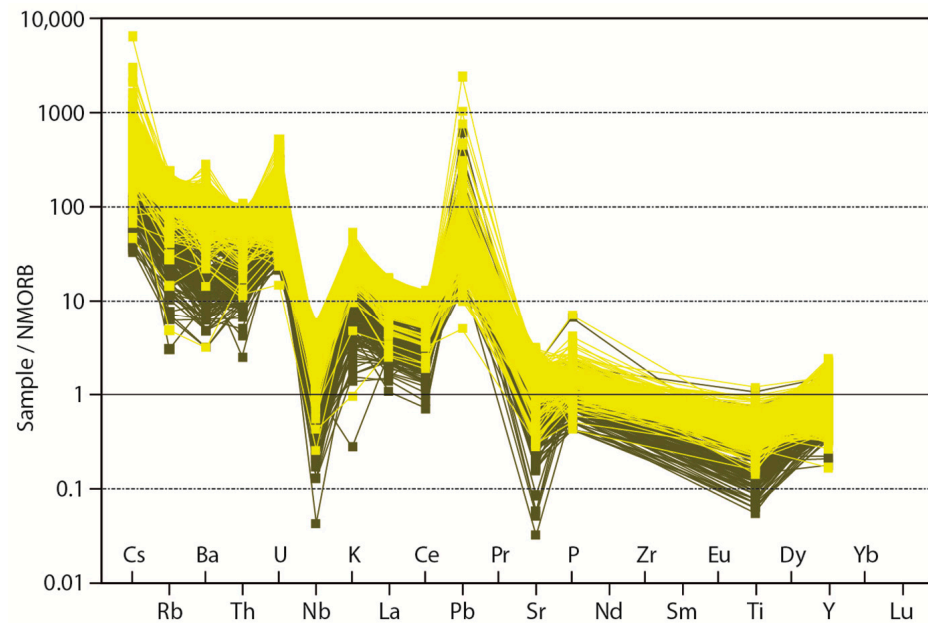


Figure 19. Spider diagram for paragneiss normalized to the N-MORB standard [56]. The yellow and green areas represent paragneisses and mineralized paragneisses, respectively.

4.3.4. Sm-Nd Isotopic Geochemistry

The Sm-Nd isotopic system provides a means of interpreting the geotectonic environment in which volcanic and sedimentary rocks were formed. Moreover, in the case of igneous rocks, it allows for the identification of the nature of the source. Both elements exhibit comparable behavior, remaining as immobile elements under weathering and moderate hydrothermal alteration conditions, which is particularly advantageous when examining rocks that have undergone partial hydrothermal alteration. Moreover, the subtle differences in their behavior make them highly effective markers of the mantle source of magmas. During partial melting, samarium (Sm) tends to concentrate in the residual mantle, whereas neodymium (Nd) tends to concentrate in the melt [57–59]. The authors put forth the hypothesis that the majority of igneous rocks were formed from a homogeneous mantle with an isotopic Sm/Nd ratio analogous to that of chondrite (CHUR: chondrite uniform reservoir). As with other isotopic systems, the isotopic relation can be represented using the notation ϵNd and is the relation between the positive and negative ϵNd values. According to [60], positive ϵNd values indicate an impoverished mantle source, while negative values indicate a crustal or enriched mantle source and a greater crustal contribution. An impoverished mantle is one that has undergone multiple partial melts, as is the case with marine sediments due to continuous MORB extrusion, which exhibit a higher Sm/Nd ratio than CHUR. Consequently, the mantle is enriched in ^{143}Nd (owing to the higher concentration of Sm), and the magmas derived from this source exhibit a higher $^{143}\text{Nd}/^{144}\text{Nd}$ ratio and positive ϵNd . In analyses of samples from the Touro deposit and vicinity, the Sm and Nd values are relatively homogeneous within each lithological group (gneisses and amphibolites), with ranges of 33.03–33.04 and 6.49–6.95 for Nd and Sm in metagreywackes and 10.23–12.15 and 3.47–3.93 in metamafic rocks, respectively. Furthermore, the narrow range of values is reflected in the $^{143}\text{Nd}/^{144}\text{Nd}$ and $^{147}\text{Sm}/^{144}\text{Nd}$ isotopic ratios, which have values of 0.511892–0.511885 and 0.1187–0.1246 for the gneisses and 0.512346–0.512394 and 0.1899–0.2054 for the igneous rocks, respectively. Each group displays highly homogeneous and clearly differentiated values (Figure 20).

For both lithological groups, the CHUR and DM model ages were calculated, which represent the extraction age of the magmas from their primordial mantle source (Figure 21). These data, when considered in conjunction with the detrital zircon ages [22], provide insight into the provenance of these materials. The calculated ages of the magmatic rocks in [17,61] are approximately 500 Ma in the Órdenes unit, which is in close agreement with

our model ages. In the case of the metasedimentary rocks, the data were plotted as ϵNd vs. time. The values obtained for the metagreywackes indicate an impoverished mantle of 1.2 Ga, which is consistent with the findings of other researchers in this field.

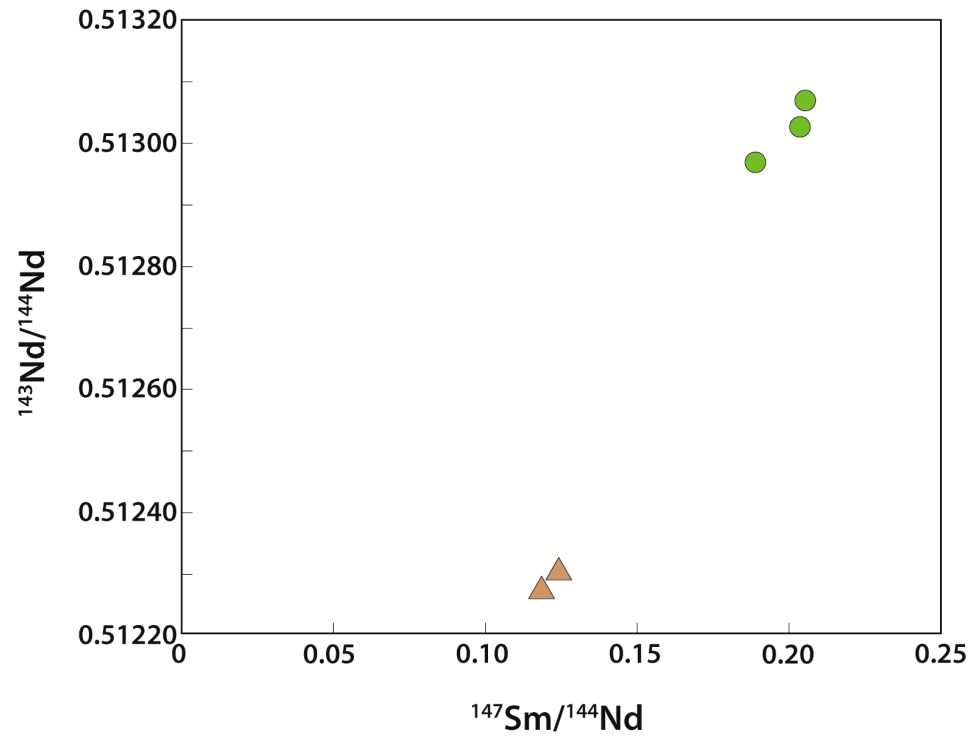


Figure 20. The $^{147}\text{Sm}/^{144}\text{Nd}$ vs. $^{143}\text{Nd}/^{144}\text{Nd}$ plot for the samples that correspond to the two main lithologies (green circles: amphibolites; brown triangles: paragneisses). The discrepancies are less significant than the symbols that have been employed.

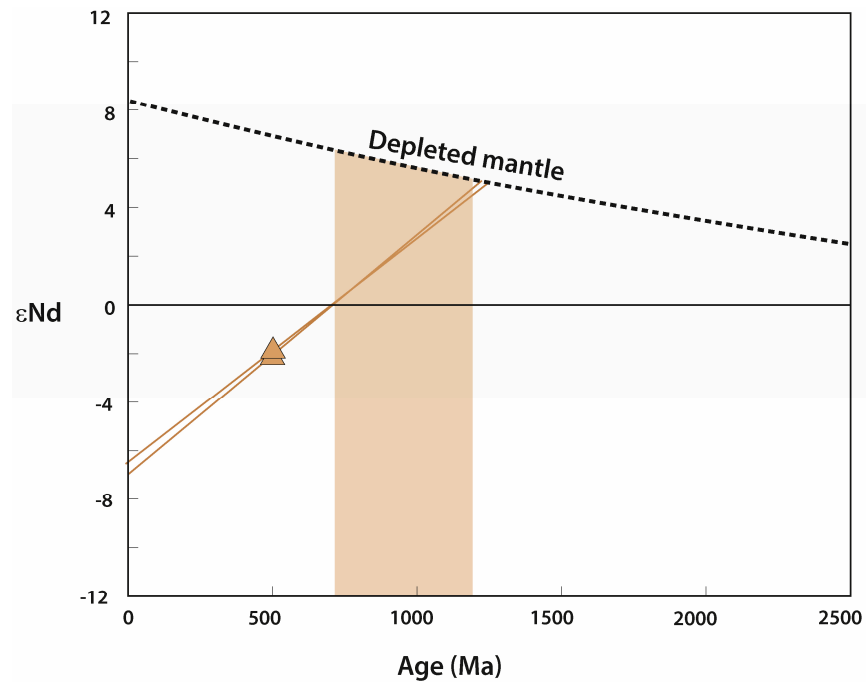


Figure 21. The TDM [59] model age for the analyzed metagreywackes of the Órdenes Complex is 500 Ma. Previously obtained model ages published in [17,61] from gneisses and basic rocks are also shown for comparison (brown band).

5. Discussion

The rocks that comprise the Touro deposit have undergone a lengthy process of genesis and evolution, occurring across three distinct periods of formation, as proposed in [1] (Table 2). Furthermore, numerous authors have previously described the geodynamic context and general characteristics of this geologic setting [4–14,19–23,27–34]. The proposed evolution commenced during the Ordovician period (approximately 480 million years ago), when siliciclastic sediments were deposited in a back-arc extensional basin setting that included the deposition of basalts and the formation of volcanic massive sulfide deposits.

Table 2. Summary of the three main periods of Touro deposit formation (modified from [1]).

Formation Period	Tectonic Setting	Process	Ore and Rocks	Structural Elements
First Step: Early Ordovician (±480 Ma)	Extensional back-arc basin setting (transtension)	Deposition of siliciclastic sediments and basalts	Formation of VMS deposits; host rocks are hydrothermally affected	Normal extensional faults
Second Step: Early Devonian (410–390 Ma)	Burial of siliciclastic sediments, mafic rocks, and VMSs	Metamorphism of siliciclastic sediments, mafic rocks, and VMSs under amphibolite facies	Transformation of rocks into amphibolites and paragneisses	Foliation in all the rocks; development of S-type mylonites; folds
Third Step: Late Devonian to Early Permian (375–295 Ma)	Exhumation of the sequence, emplacement via thrust on the top of the Ordenes Complex, and folding	Broad retrograde metamorphism	Formation of retrograde amphibolites and chlorite-rich schists	Formation of a roughly N–S-trending antiform (Arinteiro) during the last Variscan deformation

The second step [1] involved the burial of the siliciclastic sediments, mafic rocks, and VMSs at depths of approximately 10 km during the Early Devonian period (410–390 Ma). These rocks were subsequently metamorphosed under amphibolite facies, with the siliciclastic rocks undergoing a transformation into paragneisses, which may contain bands with high graphite contents (possibly black shales). Furthermore, the basaltic rocks underwent metamorphism during the aforementioned Early Devonian period, as evidenced in References [62–65]. The hydrothermally affected host rocks underwent a transformation into calcium-poor and iron-rich chlorite-garnet amphibolites, as well as mineralized paragneisses. It is therefore proposed that the anomalous, Ca-poor garnet amphibolites are the result of metamorphism affecting basalts that have previously undergone hydrothermal alteration and metasomatism. Similarly, the mineralized paragneisses are the metamorphic result of metasomatized and mineralized siliciclastic sediments. Additionally, mica growth occurs during metamorphism in paragneisses, yet the mica composition differs significantly between mineralized and non-mineralized paragneisses. The presence of sulfur in mineralized paragneisses results in the partitioning of iron toward sulfides, which leads to a notable reduction in the concentration of biotite. This phenomenon is characterized by the formation of phlogopite in place of biotite due to the lack of sufficient iron [66–68].

The third phase of regional geological evolution [1] occurred when the sequence was exhumed and positioned via a thrust on the top of the ophiolites of the Ordenes Complex during the Late Devonian period (375–371 Ma [9–11,19–23,69,70]), which resulted in extensive retrograde metamorphism, whereby the high-grade metamorphic rocks were transformed into amphibolites and chlorite-rich schists. Following the exhumation, an approximately N–S-trending antiform was formed in the Late Carboniferous–Early Permian period, known as the Arinteiro antiform (Figure 2), which was likely formed during the last Variscan deformation, as proposed in previous studies [24,25], and is associated with the Asturian oroclinal development. In accordance with Reference [1], the current contact between the amphibolites, paragneisses, and VMSs is sheared due to the disparate

rheological behaviors exhibited by these rock types. It seems probable that the VMS feeder zones are associated with the ancient Ordovician fracture system, which was formed as a result of rifting. The copper ore situated in the feeder zones and at the base of the basalt-interstratified levels has resulted in the formation of deformed stockworks (breccias) and replacements of the basalts and, on occasion, the paragneisses.

The four rock types involved in the deposit formation were previously examined from a mineralogical perspective under a microscope in [1], and our microprobe findings substantiate the conclusion that their mineralogical characteristics are dependent on the specific rock type. The garnets display three distinct compositions, contingent on their provenance, and the garnets in the amphibolites and mineralized garnet amphibolites are entirely distinct. In the mineralized rocks, the almandine is markedly Ca-poor, whereas in the amphibolite, in close proximity to the mineralized rock, the garnet is grossularite. This phenomenon can be attributed to the hydrothermal mobilization of calcium and metasomatism from the mineralized rock to the amphibolite, which undergoes a process of fine-grained and calcium-rich transformation. With regard to the amphibole composition, magnesium–hornblende gradually transforms into tremolite in the calcium-poor, mineralized garnet amphibolite, in accordance with the loss of calcium.

Feldspar analysis allowed for the differentiation between the two amphibolite types. Alkali feldspar is present in mineralized garnet amphibolites, while calcium-rich plagioclase is found in amphibolites, including those with small grossularite garnets. The micas subjected to analysis are of the biotite variety, and their plot demonstrates the distinctions between the various rocks involved. During metamorphism, the plot of the mica formed in the mineralized paragneiss is situated within the phlogopite field. In the paragneiss, the micas are predominantly biotite, and the scarce biotite present in the garnet amphibolite is also of the biotite variety, albeit richer in iron. As previously stated, the presence of sulfur in mineralized paragneisses results in the partitioning of iron toward sulfides. This phenomenon causes the formation of phlogopite in place of biotite due to the lack of sufficient iron [66–68]. The secondary minerals include chlorite (ripidolite) and epidote–clinozoisite. Chlorites are exclusively present in mineralized rocks, with those derived from garnet amphibolites exhibiting higher iron contents than those derived from mineralized paragneisses.

In terms of the whole-rock chemical analysis, the four defined rocks can be grouped into the following categories.

The non-mineralized igneous rock plots utilized in this study, including the Hf–Th–Nb diagram [54], indicate that the majority of samples fall within the E-MORB and intraplate tholeiitic fields, which is consistent with the back-arc tectonic setting proposed in [9,18]. The other diagrams employed to ascertain the tectonic setting of the mafic rocks indicate that these rocks are subalkaline in nature ($\text{Na}_2\text{O} + \text{K}_2\text{O}$ vs. MgO), corresponding to a tholeiitic series (AFM), with the majority of the samples plotting in close proximity to the FeO–MgO side of the diagram. These findings, in conjunction with the Th–Co plot, suggest that the samples are situated at the boundary between the calc-alkaline and tholeiitic fields previously proposed in [16], which is consistent with the back-arc tectonic setting.

Furthermore, the $100 \times \text{K}_2\text{O}/\text{Na}_2\text{O} + \text{K}_2\text{O}$ vs. $\text{Na}_2\text{O} + \text{K}_2\text{O}$ plot of the unaltered mafic samples indicates some degree of variability in a subset of samples. However, the majority of these minimally altered mafic samples display characteristics consistent with those of the unaltered samples.

As observed with the Th and Ba + Sr, a small number of samples were inadequately classified. The application of a multielement diagram normalized to the N-MORB standard [56] suggests the involvement of subduction tectonics, with the generation of a magmatic arc and back-arc basin.

With regard to the sedimentary rocks, the binary graph demonstrates notable increases in the Th and Pb concentrations, accompanied by negative anomalies in the Nb and Sr levels, which suggests a clear correlation with materials originating from a volcanic arc. A multielement diagram normalized to the N-MORB standard [56] with paragneiss is analo-

gous to that of the mafic rocks, exhibiting the highest fractionation but identical anomalies. These diagrams corroborate the hypothesis that the source of these metasediments is a volcanic arc.

The mineralization process affects both igneous and metasedimentary rocks. In this regard, it is notable that the mineralized igneous rocks correspond to garnet-rich amphibolites, which exhibit the geochemical feature of Ca-poor composition. The distinction between mafic and metasedimentary rocks, as well as their differentiation from mineralized rocks, can be facilitated by the use of specific trace elements, which allows for a more effective differentiation between igneous and metasedimentary rocks. The thorium contents in the paragneisses are in excess of 2 ppm (up to 14), whereas in the amphibolites, they are invariably below this value (2 ppm). The mineralized paragneisses exhibit a gradual decline in their Th contents, reaching a threshold below 1 ppm. The Ba + Sr contents in the amphibolites exceed 100 ppm, exhibiting a gradual decline to 10 ppm in garnet amphibolites concomitant with the loss of Ca. As previously stated, the rock classification was conducted during the visual core logging, which may have resulted in the inclusion of some rare samples that were incorrectly assigned to inappropriate fields.

The transformation of the rocks during the mineralization process is progressive, as evidenced by the FeO + MgO vs. TiO₂ and Al/(Al + Fe + Mn) vs. Fe/Ti plots [1,49,50]. The plots illustrate the transition from MORB or sediments to rocks with compositions that are similar to those of metalliferous oceanic sediments. Furthermore, the plots illustrate a substantial overlap between the non-mineralized samples identified as amphibolites and those identified as paragneisses, which is indicative of the volcanic–sedimentary nature of these materials that were formed in a back-arc geotectonic context.

In the context of exploration guides, two distinct types can be identified: mineralogical and geochemical. With regard to mineralogy, the occurrence of almandine-type garnet in amphibolites is a reliable indicator of the mineralized type. In contrast, the presence of grossularite is exclusive to non-mineralized amphibolites situated in the transition zone between mineralized and non-mineralized formations. The type of mica can also be useful in distinguishing between mineralized paragneisses (phlogopite) and non-mineralized paragneisses (biotite). In addition, it has been demonstrated that specific elements are highly effective in differentiating between the four principal types of rocks, particularly in the case of Th. The content of this element is entirely distinct in amphibolites compared to paragneisses, and it gradually diminishes in paragneisses with increasing mineralization. Subsequently, the differentiation of these three lithological types is contingent upon the Th content (Figure 4). Furthermore, the concentration of Ba + Sr enables the distinction between amphibolites and garnet-amphibolites (mineralized amphibolites) (Figures 4 and 5). These three elements are now being employed as exploration guides. In this regard, the diagram in Figure 9 [49–51] is also of great utility.

In the Iberian Peninsula, there is another important VMS district: the Iberian Pyrit Belt (IPB). A broad discussion comparing the Touro area and IPB is made in [1], and the authors conclude that both are VMS deposits but of different types [15] (Touro is siliciclastic–mafic and the IPB is bimodal siliciclastic), formed in different geodynamic contexts and different moments (the Ordovician and Carboniferous periods, respectively).

6. Conclusions

The Touro deposit is a volcanic massive sulfide (VMS) deposit of the siliciclastic–mafic type, formed in a back-arc geological environment during the Ordovician period (approximately 480 million years ago). The ore is predominantly associated with mafic rocks, which underwent metasomatism due to the influence of hydrothermal fluids, resulting in a notable depletion of calcium and an increase in iron. The siliciclastic rocks were also mineralized, albeit to a lesser extent, and underwent metasomatism, resulting in an increase in Fe and a loss of Al, alkalis, Ba, and Sr. From a geochemical perspective, the Th contents in mafic (less than 2 ppm) and sedimentary (greater than 2 ppm) rocks are distinct, allowing for a clear differentiation between the two. Additionally, a notable Th

loss is observed in paragneiss during the mineralization process. Furthermore, the loss of Ba and Sr during mineralization allows for the differentiation between amphibolites and mineralized, garnet-rich amphibolites.

During the Early Devonian period (410–390 Ma), the hydrothermally affected host rocks underwent significant transformation, resulting in the formation of calcium-poor and iron-rich chlorite-garnet amphibolites, as well as mineralized paragneisses. This process also resulted in the formation of a foliation in all the rocks, which gave rise to S-type mylonites. In addition to the high-grade metamorphic event, pyrite was transformed into pyrrhotite, and the ore was completely recrystallized, exhibiting exceptional Co concentrations in both pyrrhotite and chalcopyrite. From the Late Devonian to Late Carboniferous–Early Permian period (375–295 Ma), the sequence was exhumed and placed on top of the Órdenes Complex ophiolites via a thrust fault. A retrometamorphic event occurred, whereby the high-grade metamorphic rocks underwent a transformation into amphibolites and chlorite-rich schists. In conclusion, an N–S-trending antiform was formed during the final Variscan deformation stage.

The geochemical characterization of the mineralogy and the host rocks of the giant Touro Cu deposit, which has undergone intense high-grade metamorphism and subsequent retrograde metamorphism during its exhumation, has facilitated the recognition of its geological history and geodynamic formation environment, enabling the establishment of exploration guidelines for this world-class mafic–siliciclastic VMS deposit type, which is located in the northwest of the Iberian Peninsula.

Supplementary Materials: The following supporting information can be downloaded at <https://www.mdpi.com/article/10.3390/min14111159/s1>, Supplementary A to G. Supplementary A: The results of the analysis of the major and trace elements in the amphibolite samples. Supplementary B: The results of the analysis of the major and trace elements in the garnet amphibolite samples. Supplementary C: The results of the analysis of the major and trace elements in the paragneiss samples. Supplementary D: The results of the analysis of the major and trace elements in the mineralized paragneiss samples. Supplementary E: the results of the analysis of the major and trace elements analyzed for mineral characterization via EPMA. Supplementary F: The results of the analysis of the major and trace elements in the 27 unaltered samples collected by us. Supplementary G: Figure illustrating the bivariate X–Y plots.

Author Contributions: Conceptualization, P.N., A.M.-I. and D.A.; methodology, P.N., A.R. and J.F.-B.; software, A.R. and J.F.-B.; validation, P.N., A.R., D.A., A.M.-I. and F.D.-R.; formal analysis, P.N., A.R., and J.F.-B.; investigation, P.N., A.R. and J.F.-B.; resources, F.D.-R., F.C., D.A. and A.M.-I.; data curation, A.R., D.A., J.F.-B. and P.N.; writing—original draft preparation, A.M.-I.; writing—review and editing, D.A., P.N., J.F.-B. and A.R.; visualization, A.R., J.F.-B. and P.N.; supervision, A.M.-I., P.N., D.A. and A.R.; project administration, A.M.-I. and D.A.; funding acquisition, P.N., D.A., A.M.-I., F.D.-R. and F.C. All authors have read and agreed to the published version of the manuscript.

Funding: This research was partially funded by Ministerio de Economía, Industria y Competitividad, Gobierno de España, project CGL2016-76532R (AEI/FEDER/UE).

Data Availability Statement: The analytical data included in this publication are presented in the Supplementary Materials.

Acknowledgments: The authors are grateful to Atalaya Mining and Cobre San Rafael S.A. for access to the drilling cores, logs, and other data provided, and to their geological staff for their assistance with the core logging and geological knowledge of the study area. We also want to thank the old staff of the Lundin Department of Geology for their drill core logs, geochemical analyses, and contribution to the knowledge of this area of world relevance. Furthermore, we would like to extend our gratitude to Sam Wright and Tom Meuzelaar (Life Cycle Geo, LLC) for their invaluable assistance with the statistical data treatment. The authors are thankful for the technical and human support provided by SGIker of the UPV/EHU and European funding (ERDF and ESF). We are grateful to Miguel A. Fernández-González at SCT of the University of Oviedo, who provided valuable assistance with the technical aspects of the EPMA trace element analysis and imaging. We are also grateful to the

three anonymous reviewers for their comments and suggestions that greatly improved the clarity and quality of this paper.

Conflicts of Interest: Authors Pablo Nuñez, Fernando Cortés and Fernando Díaz-Riopa were employed by the company Cobre San Rafael, S.L. The remaining authors declare that the research was conducted in the absence of any commercial or financial relationships that could be construed as a potential conflict of interest.

References

1. Arias, M.; Nuñez, P.; Arias, D.; Gumiel, P.; Castañón, C.; Fuertes-Blanco, J.; Martin-Izard, A. 3D Geological Model of the Touro Cu Deposit, A World-Class Mafic-Siliciclastic VMS Deposit in the NW of the Iberian Peninsula. *Minerals* **2021**, *11*, 85. [[CrossRef](#)]
2. Meuzelaar, T.; Núñez-Fernández, P.; Martín-Izard, A.; Arias-Prieto, D.; Díaz-Riopa, F. The waste rock of the Touro copper deposit in Galicia, Spain: Challenges for its environmental characterization. *Geochem. Explor. Environ. Anal.* **2021**, *21*, geochem2020-081. [[CrossRef](#)]
3. Núñez, P.; Watts, T.; Martin-Izard, A.; Arias, D.; Rubio, Á.; Cortés, F.; Díaz-Riopa, F. Airborne Electromagnetic Survey over the Touro Copper VMS World Class Deposit (NW Spain): Geological and Geophysical Correlation. *Minerals* **2023**, *13*, 17. [[CrossRef](#)]
4. Badham, P.; Williams, J. Genetic and Exploration Models for Sulfide Ores in Metaophiolites, Northwest Spain. *Econ. Geol.* **1981**, *76*, 2118–2127. [[CrossRef](#)]
5. Sides, E.J. An alternative approach to the modelling of deformed stratiform and stratabound deposits. In Proceedings of the Twentieth International Symposium on the Application of Computers and Mathematics in the Mineral Industries, APCOM 87, Johannesburg, South Africa, 19–23 October 1987; Volume 3, Geostatistics. pp. 187–198.
6. Serranti, S.; Ferrini, V.; Masi, U.; Nicoletti, M.; Conde, L. Geochemical features of the massive sulfide (Cu) metamorphosed deposit of Arinteiro (Galicia, Spain) and genetic implications. *Period. Mineral.* **2002**, *71*, 27–48.
7. Williams, P.J. The genesis and metamorphism of the Arinteiro-Bama Cu deposits, Santiago de Compostela, northwestern Spain. *Econ. Geol.* **1983**, *78*, 1689–1700. [[CrossRef](#)]
8. Castiñeiras, P. Origen y Evolución Tectonotermal de las Unidades de o Pino y Cariño (Complejos Alóctonos de Galicia). Ph.D. Thesis, Universidad Complutense de Madrid, Madrid, Spain, 2005. Serie Terra Nova 28. p. 289.
9. Arenas, R.; Sánchez Martínez, S.; Díez Fernández, R.; Gerdes, A.; Abati, J.; Fernández-Suárez, J.; Andonaegui, P.; González Cuadra, P.; López Carmona, A.; Albert, R.; et al. Allochthonous terranes involved in the Variscan suture of NW Iberia: A review of their origin and tectonothermal evolution. *Earth Sci. Rev.* **2016**, *161*, 140–178. [[CrossRef](#)]
10. Barreiro, J.G.; Martínez Catalán, J.R.; Fernández, R.D.; Arenas, R.; García, F.D. Upper crust reworking during gravitational collapse: The Bembibre-Pico Sacro detachment system (NW Iberia). *J. Geol. Soc.* **2010**, *167*, 769–784. [[CrossRef](#)]
11. Díez Fernández, R.; Martínez Catalán, J.R.; Arenas Martín, R.; Abati Gómez, J. Tectonic evolution of a continental subduction-exhumation channel: Variscan structure of the basal allochthonous units in NW Spain. *Tectonics* **2011**, *30*, TC3009. [[CrossRef](#)]
12. Julivert, M.; Martínez, F.J. The Structure and Evolution of the Hercynian Fold Belt in the Iberian Peninsula. In *The Anatomy of Mountain Ranges, Princeton Legacy Library and Princeton Series in Geology and Paleontology*, 788; Schaer, J.-P., Rodgers, J., Eds.; Princeton University Press: Princeton, NJ, USA, 2014; Chapter 6; pp. 65–105.
13. Farias, P.; Gallastegui, G.; González Lodeiro, F.; Marquín, J.; Martín Parra, L.M.; De Pablo Macía, J.G.; Rodríguez Fernández, L.R. Aportaciones al conocimiento de la litoestratigrafía y estructura de Galicia Central. *Mem. Fac. Ciências Univ. Porto* **1987**, *1*, 411–431.
14. Martínez Catalán, J.R.; Álvarez Lobato, F.; Pinto, V.; Gómez Barreiro, J.; Ayarza, P.; Villalaín, J.J.; Casas, A. Gravity and magnetic anomalies in the allochthonous Ordenes Complex (Variscan belt, northwest Spain): Assessing its internal structure and thickness. *Tectonics* **2012**, *31*, TC5007. [[CrossRef](#)]
15. Galley, A.G.; Hannington, M.D.; Jonasson, I.R. Volcanogenic Massive Sulphide Deposits. In *Mineral Deposits of Canada—A Synthesis of Major Deposit-Types, District Metallogeny, the Evolution of Geological Provinces, and Exploration Methods: Geological Association of Canada. Ontario, Canada. Mineral Deposits Division; Goodfellow, W.D., Ed.; Special Publication; Society of Economic Geologists: Littleton, CO, USA, 2007; Volume 5, pp. 141–161.*
16. Andonaegui, P.; Arenas, R.; Albert, R.; Sánchez Martínez, S.; Díez Fernández, R.; Gerdes, A. The last stages of the Avalonian–Cadomian arc in NW Iberian Massif: Isotopic and igneous record for a long-lived peri-Gondwanan magmatic arc. *Tectonophysics* **2016**, *681*, 6–14. [[CrossRef](#)]
17. Fuenlabrada, J.M.; Arenas, R.; Martínez, S.S.; García, F.D.; Castiñeiras, P. A peri-Gondwanan arc in NW Iberia: Isotopic and geochemical constraints on the origin of the arc—A sedimentary approach. *Gondwana Res.* **2010**, *17*, 338–351. [[CrossRef](#)]
18. Sánchez Martínez, S.; Arenas, R.; Albert, R.; Gerdes, A.; Fernández-Suárez, J. *Updated Geochronology and Isotope Geochemistry of the Vila de Cruces Ophiolite: A Case Study of a Peri-Gondwanan Back-Arc Ophiolite*; Special Publications 503; Geological Society: London, UK, 2021; pp. 497–530. [[CrossRef](#)]

19. Díez-Fernández, R.; Arenas, R.; Francisco-Pereira, M.; Sánchez-Martínez, S.; Albert, R.; Martín Parra, L.M.; Rubio Pascual, F.J.; Matas, J. Tectonic evolution of Variscan Iberia: Gondwana–Laurussia collision revisited. *Earth Sci. Rev.* **2016**, *162*, 269–292. [[CrossRef](#)]
20. Martínez Catalán, R.; Arenas, R.; García, F.D.; Abati, J. Variscan accretionary complex of northwest Iberia: Terrane correlation succession of tectonothermal events. *Geology* **1997**, *25*, 1103–1106. [[CrossRef](#)]
21. Ziegler, P.A. (Ed.) Hercynian Suturing of Pangea. In *AAPG Memoir Vol 43: Evolution of the Arctic-North Atlantic and the Western Tethys*; The American Association of Petroleum Geologists: Tulsa, OK, USA, 1988; pp. 25–32.
22. Albert, R.; Arenas, R.; Gerdes, A.; Sánchez Martínez, S.; Fernández-Suárez, J.; Fuenlabrada, J.M. Provenance of the Variscan Upper Allochthon (Cabo Ortegal Complex, NW Iberian Massif). *Gondwana Res.* **2015**, *28*, 1434–1448. [[CrossRef](#)]
23. Andonaegui, P.; Sánchez-Martínez, S.; Castiñeiras, P.; Abati, J.; Arenas, R. Reconstructing subduction polarity through the geochemistry of mafic rocks in a Cambrian magmatic arc along the Gondwana margin (Órdenes Complex, NW Iberian Massif). *Int. J. Earth Sci.* **2016**, *105*, 713–725. [[CrossRef](#)]
24. Gutiérrez-Alonso, G.; Collins, A.S.; Fernández-Suárez, J.; Pastor-Galán, D.; González-Clavijo, E.; Jourdan, F.; Weil, A.B.; Johnston, S.T. Dating of lithospheric buckling: $40\text{Ar}/39\text{Ar}$ ages of syn-orocline strike-slip shear zones in northwestern Iberia. *Tectonophysics* **2015**, *643*, 44–54. [[CrossRef](#)]
25. Pastor-Galán, D.; Gutiérrez-Alonso, G.; Murphy, J.B.; Fernández-Suárez, J.; Hofmann, M.; Linnemann, U. Provenance analysis of the Paleozoic sequences of the northern Gondwana margin in NW Iberia: Passive margin to Variscan collision and orocline development. *Gondwana Res.* **2013**, *23*, 1089–1103. [[CrossRef](#)]
26. Noblet, C.; Lefort, J.P. Sedimentological evidence for a limited separation between Armorica and Gondwana during the Early Ordovician. *Geology* **1990**, *18*, 303–306. [[CrossRef](#)]
27. Díez Fernández, R.; Martínez Catalán, J.R.; Arenas, R.; Abati, J.; Gerdes, A.; Fernández-Suárez, J. U–Pb detrital zircon analysis of the lower allochthon of NW Iberia: Age constraints, provenance and links with the Variscan mobile belt and Gondwanan cratons. *J. Geol. Soc.* **2012**, *169*, 655–665. [[CrossRef](#)]
28. Martínez Catalán, J.R.; Arenas, R.; Abati, J.; Martínez, S.S.; García, F.D.; Suárez, J.F.; Cuadra, P.G.; Castiñeiras, P.; Barreiro, J.G.; Montes, A.D.; et al. A rootless suture and the loss of the roots of a mountain chain: The Variscan belt of NW Iberia. *Comptes Rendus Geosci.* **2009**, *341*, 114–126. [[CrossRef](#)]
29. Scotese, C.R.; Boucot, A.J.; Mckerrow, W.S. Gondwanan palaeogeography and palaeoclimatology. *J. Afr. Earth Sci.* **1999**, *28*, 99–114. [[CrossRef](#)]
30. Arenas, R.; Sánchez Martínez, S.; Gerdes, A.; Albert, R.; Díez Fernández, R.; Andonaegui, P. Re-interpreting the Devonian ophiolites involved in the Variscan suture: U–Pb and Lu–Hf zircon data of the Moeche Ophiolite (Cabo Ortegal Complex, NW Iberia). *Int. J. Earth Sci.* **2014**, *103*, 1385–1402. [[CrossRef](#)]
31. Van Zuuren, A. Structural petrology of an area near Santiago de Compostela (NW Spain). *Leidse Geol. Meded.* **1970**, *45*, 1–71.
32. Castiñeiras, P. Origen y Evolución Tectonotermal de las Unidades de o Pino y Cariño (Complejos Alóctonos de Galicia). Ph.D. Thesis, Universidad Complutense de Madrid, Madrid, Spain, 2003.
33. Martínez Catalán, J.R.; Díaz García, F.; Arenas, R.; Abati, J.; Castiñeiras, P.; González Cuadra, P.; Gómez Barreiro, J.; Rubio Pascual, F.J. Thrust and detachment systems in the Ordenes Complex (northwestern Spain) implications for the Variscan-Appalachian geodynamics. In *Variscan-Appalachian Dynamics: The Building of the Late Paleozoic Basement*; Martínez Catalán, J.R., Hatcher, R.D., Jr., Arenas, R., Díaz García, F., Eds.; Special Paper; Geological Society of America: Boulder, CO, USA, 2002; Volume 364, pp. 163–182.
34. Marcos, A.; Marquínez, J.; Perez-Estaún, A.; Pulgar, J.; Bastida, F. Nuevas aportaciones al conocimiento de la evolución tectonometamórfica del complejo de Cabo Ortegal (NW de España). *Cuad. Lab. Xeolóxico Laxe* **1984**, *7*, 125–137.
35. Castroviejo, R.; Armstrong, E.; Lago, A.; Martínez Simón, J.M.; Argüelles, A. Geología de las mineralizaciones de sulfuros masivos en los cloritoesquistos de Moeche (complejo de Cabo Ortegal, A Coruña). *Bol. Geol. Min.* **2004**, *115*, 3–34.
36. Arenas, R.; Catalán, J.R.M. Prograde Development of Corona Textures in Metagabbros of the Sobrado Unit (Ordenes Complex, Northwestern Iberian Massif). *Spec. Pap. Geol. Soc. Am.* **2002**, *364*, 73–88.
37. Gil Ibarguchi, J.I.; Arenas, R. Metamorphic Evolution of the Allochthonous Complexes from the Northwest of Iberian Peninsula. In *Pre-Mesozoic Geology of Iberia*; Dallmeyer, R.D., Martínez-García, E., Eds.; Springer: Berlin/Heidelberg, Germany, 1990; pp. 237–246.
38. Catalán, J.M.; Martín, R.A. Deformación extensional de las unidades alóctonas superiores de la parte oriental del Complejo de Ordenes (Galicia). *Geogaceta* **1992**, *11*, 108–111.
39. Available online: <https://atalayamining.com/es/operaciones/proyecto-touro/> (accessed on 13 November 2024).
40. García de Madinabeitia, S.; Sánchez Lorda, M.E.; Gil Ibarguchi, J.I. Simultaneous determination of major to ultratrace elements in geological samples by fusion-dissolution and inductively coupled plasma mass spectrometry techniques. *Anal. Chim. Acta* **2008**, *625*, 117–130. [[CrossRef](#)]
41. Miller, J.N.; Miller, J.C. *Statistics and Chemometrics for Analytical Chemistry*, 6th ed.; Pearson Education: Toronto, ON, Canada, 2004; p. 296.

42. Pin, C.; Santos Zalduegui, J.F. Sequential separation of light rare-earth elements, thorium and uranium by miniaturized extraction chromatography: Application to isotopic analyses of silicate rocks. *Anal. Chim. Acta* **1997**, *339*, 79–89. [[CrossRef](#)]
43. Fernandez, F.J.; Marcos, A. Mylonitic Foliation Developed by Heterogeneous Pure Shear Under High-Grade Conditions in Quartz Feldspathic Rocks (*Chimparra gneiss* Formation, Cabo Ortegal Complex, NW Spain). In *Basement Tectonics 11 Europe and Other Regions*; Springer: Berlin/Heidelberg, Germany, 1996; pp. 17–34.
44. Hawthorne, C.; Oberti, R.; Harlow, G.; Maresch, W.; Martin, R.; Schumacher, J.; Welch, M. Nomenclature of the amphibole supergroup. *Am. Mineral.* **2012**, *97*, 2031–2048. [[CrossRef](#)]
45. Leake, B. Nomenclature of amphibole: Report of the Subcommittee on amphiboles of the International Commission on New Mineral and Mineral Names. *Can. Mineral.* **1997**, *35*, 219–247.
46. Hey, M. A new review of the chlorites. *Mineral. Mag.* **1954**, *30*, 277–292. [[CrossRef](#)]
47. Grapes, R.; Hoskin, P. Epidote group minerals in low-medium pressure metamorphic terranes. *Rev. Mineral. Geochem.* **2004**, *56*, 301–345. [[CrossRef](#)]
48. Cathelineau, M.; Izquierdo, G. Temperature-composition relationships of autigenic micaceous minerals in the Los Azufres geothermal system. *Contrib. Mineral. Petrol.* **1988**, *100*, 418–428. [[CrossRef](#)]
49. Boström, K. Origin and Fate of Ferromanganoan Active Ridge Sediments. In *Pelagic Sediments: On Land and Under the Sea*; Wiley: Hoboken, NJ, USA, 1975; p. 401. [[CrossRef](#)]
50. Spry, P.G.; Peter, J.M.; Slack, J.F. *Meta-Exhalites as Exploration Guides to Ore: Reviews in Economic Geology*; Society of Economic Geologists: Lyttelton, CO, USA, 1998; Volume 11, pp. 163–201.
51. Peter, J.M.; Goodfellow, W.D.; Doherty, W. Hydrothermal Sedimentary Rocks of the Heath Steele Belt, Bathurst Mining Camp, New Brunswick: Part 2. Bulk and Rare Earth Element Geochemistry and Implications for Origin. *Econ. Geol. Monogr.* **2003**, *11*, 391–415.
52. Irvine, T.N.; Baragar, W.R.A. A guide to the chemical classification of the common volcanic rocks. *Can. J. Earth Sci.* **1971**, *8*, 523–548. [[CrossRef](#)]
53. Hastie, A.R.; Kerr, A.C.; Pearce, J.A.; Mitchell, S.F. Classification of Altered Volcanic Island Arc Rocks using Immobile Trace Elements: Development of the Th Co Discrimination Diagram. *J. Petrol.* **2007**, *48*, 2341–2357. [[CrossRef](#)]
54. Wood, D.A. The application of a Th-Hf-Ta diagram to problems of tectonomagmatic classification and to establishing the nature of crustal contamination of basaltic lavas of the British Tertiary Volcanic Province. *Earth Planet Sci. Lett.* **1980**, *50*, 11–30. [[CrossRef](#)]
55. Pearce, J.A.; Cann, J.R. Tectonic setting of basic volcanic rocks determined using trace element analyses. *Earth Planet Sci. Lett.* **1973**, *19*, 290–300. [[CrossRef](#)]
56. Sun, S.S.; McDonough, W.F. Chemical and isotopic systematics of oceanic basalts: Implications for mantle composition and processes. *Magmat. Ocean. Basins. Geol. Soc.* **1989**, *42*, 313–345. [[CrossRef](#)]
57. DePaolo, D.J.; Wasserburg, G.J. Inferences about Magma Sources and Mantle Structure from Variations of $^{143}\text{Nd}/^{144}\text{Nd}$. *Geophys. Res. Lett.* **1976**, *3*, 743–746. [[CrossRef](#)]
58. DePaolo, J. *Neodymium Isotope Geochemistry: An Introduction*; Springer-Verlag: New York, NY, USA, 1988.
59. Wasserburg, G.J.; Jacobsen, S.B.; DePaolo, D.J.; McCulloch, M.T.; Wen, T. Precise determination of Sm/Nd ratios, Sm and Nd isotopic abundances in standard solutions. *Geochim. Cosmochim. Acta* **1981**, *45*, 2311–2323. [[CrossRef](#)]
60. Dickin, A.P. *Radiogenic Isotope Geology*, 2nd ed.; Cambridge University Press: Cambridge, UK, 2005.
61. Fuenlabrada, J.M.; Arenas, R.; Martínez, S.S.; Fernández, R.D.; Pieren, A.P.; Pereira, M.F.; Chichorro, M.; Silva, J.B. Geochemical and isotopic (Sm-Nd) provenance of Ediacaran–Cambrian metasedimentary series from the Iberian Massif. Paleoreconstruction of the North Gondwana margin. *Earth Sci. Rev.* **2019**, *201*, 103079. [[CrossRef](#)]
62. Santos Zalduegui, J.F.; Scharer, U.; Gil Ibarra, J.I.; Girardeau, J. Origin and evolution of the Paleozoic Cabo Ortegal ultramafic complex (NW Spain): U-Pb, Rb-Sr and Pb-Pb isotope data. *Chem. Geol.* **1996**, *129*, 281–304. [[CrossRef](#)]
63. Ordóñez Casado, B.; Gebauer, D.; Schafer, H.J.; Gil Ibarra, J.I.; Peucat, J.J. A single Devonian subduction event for the HP/HT metamorphism of the Cabo Ortegal complex within the Iberian Massif. *Tectonophysics* **2001**, *332*, 359–385. [[CrossRef](#)]
64. Fernández-Suárez, J.; Corfu, F.; Arenas, R.; Marcos, A.; Martínez Catalán, J.R.; Díaz García, F.; Abati, J.; Fernández, F.J. U-Pb evidence for a polyorogenic evolution of the HPHT units of the NW Iberian Massif. *Contrib. Miner. Petrol.* **2002**, *143*, 236–253.
65. Fernández-Suárez, J.; Arenas, R.; Abati, J.; Martínez Catalán, J.R.; Whitehouse, M.J.; Jeffries, T.E. U-Pb chronometry of polymetamorphic high-pressure granulites: An example from the allochthonous terranes of the NW Iberian Variscan belt. *Geol. Soc. Am. Mem.* **2007**, *200*, 469–488.
66. Nesbitt, B.E. Oxide-sulfide-silicate equilibria associated with metamorphosed ore deposits; Part II, Pelitic and felsic volcanic terrains. *Econ. Geol.* **1986**, *81*, 841–856. [[CrossRef](#)]
67. Mungall, J.E. Kinetic Controls on the Partitioning of Trace Elements Between Silicate and Sulfide Liquids. *J. Petrol.* **2002**, *43*, 749–768. [[CrossRef](#)]
68. Steenstra, E.S.; Trautner, V.T.; Berndt, J.; Klemme, S.; van Westrenen, W. Trace element partitioning between sulfide-, metal- and silicate melts at highly reduced conditions: Insights into the distribution of volatile elements during core formation in reduced bodies. *Icarus* **2020**, *335*, 113408. [[CrossRef](#)]

69. Dallmeyer, R.D.; Martínez Catalán, J.R.; Arenas, R.; Gil Ibarguchi, J.I.; Gutiérrez-Alonso, G.; Farias, P.; Bastida, F.; Aller, J. Diachronous Variscan tectonothermal activity in the NW Iberian Massif: Evidence from $^{40}\text{Ar}/^{39}\text{Ar}$ dating of regional fabrics. *Tectonophysics* **1997**, *277*, 307–337. [[CrossRef](#)]
70. Gómez Barreiro, J.; Wijbrans, J.R.; Castineiras, P.; Martínez Catalán, J.R.; Arenas, R.; Díaz García, F.; Abati, J. $^{40}\text{Ar}/^{39}\text{Ar}$ laser probe dating of mylonitic fabrics in a polyorogenic terrane of NW Iberia. *J. Geol. Soc.* **2006**, *163*, 61–73. [[CrossRef](#)]

Disclaimer/Publisher’s Note: The statements, opinions and data contained in all publications are solely those of the individual author(s) and contributor(s) and not of MDPI and/or the editor(s). MDPI and/or the editor(s) disclaim responsibility for any injury to people or property resulting from any ideas, methods, instructions or products referred to in the content.